

CrossMark  
click for updates

Cite this: DOI: 10.1039/c4sm02053g

# On the rheology of pendular gels and morphological developments in paste-like ternary systems based on capillary attraction†

Trystan Domenech and Sachin S. Velankar\*

We investigate capillary bridging-induced gelation phenomena in silica particle suspensions and pastes, where a particle-wetting fluid is added as the third component. Increasing the wetting fluid loading in the ternary system induces a morphological transition from a *pendular* network to *compact capillary aggregates* network, with an intermediate *funicular* state. To our knowledge, the formation of percolated structures from compact capillary aggregates when the volume fraction of a wetting fluid approaches that of the particles is unprecedented. Such structures appear to result from the arrested coalescence of compact capillary aggregates due to the balance between the Laplace pressure and solid-like properties (yield stress, elasticity) of the aggregates. Shear-induced yielding of the ternary systems, linked to their percolating nature, is strongly influenced by the amount of wetting fluid phase. A non-monotonic dependence of the yield stress on the amount of wetting fluid is found, with the maximum yield stress obtained for a wetting fluid-to-particle volume fraction ratio of 0.2–0.3. For pendular systems, linear viscoelastic properties display a soft glassy rheological behavior above the percolation threshold (around 4 vol% particles), and complex viscosity data can be scaled using the high frequency plateau value, as well as a single characteristic relaxation time, which decreases when the particle concentration is increased. In addition, the particle concentration dependence of the yielding transition in the pendular regime appears to be efficiently described by two parameters extracted from the steady state flow curves: the yield stress and the limiting viscosity at a high shear rate. Although these non-colloidal networks result from flow-driven assembly, the scaling laws for our pendular gels are reminiscent of colloidal gels with a fractal geometry. Our studies pinpoint new pathways to create physical gels where the interparticle attraction strength is determined by capillary interactions.

Received 13th September 2014  
Accepted 11th December 2014

DOI: 10.1039/c4sm02053g

www.rsc.org/softmatter

## 1. Introduction

The complex flow behaviors of many soft materials, such as suspensions, emulsions and colloids, have attracted considerable attention in the scientific literature. Such materials are ubiquitous in various industrial applications, such as food, cosmetic, care products and paints, where their processing strongly depends on their flow behavior. These systems can undergo gelation *via* physical or chemical routes<sup>1</sup> and the resulting arrested state exhibits typical solid-like flow dynamics, which strongly depend on the interparticle attractive energy and the volume fraction of the dispersed phase.<sup>2</sup> However, the application of a shear flow can lead to a liquid-like behavior, and the concept of yield stress<sup>3</sup> is often used to describe the solid-to-fluid transition. Recently, the use of capillary forces in near hard-sphere particle suspensions has shown a tremendous

impact on the resulting rheological properties,<sup>4,5</sup> where quasi-Newtonian simple suspensions turn into yielding viscoelastic materials due to their newfound percolating microstructure. The latter effect is observed when a small quantity of a second liquid phase, immiscible with the continuous phase, is added to the suspension. This phenomenon arises from the formation of small capillary bridges, which induces strong cohesive forces between the particles, and was reported for small-molecule liquids<sup>4,6–8</sup> and immiscible polymer<sup>5</sup> systems. A similar situation is well-known in granular media, where the addition of a wetting liquid in small proportions confers great strength and stability to a granular pile.<sup>9,10</sup> The physical binding of solid bodies is primarily driven by the surface tension of interstitial liquid bridges<sup>11</sup> and greatly affects the typical properties of the granular pile such as surface angle of repose and size segregation.<sup>12</sup> However, the variation in material strength is not monotonic with that of the liquid content:<sup>9,13</sup> while the cohesion of the granular media is substantially increased up to a certain amount of added liquid, higher liquid contents will soften the material and decrease its stability, which can lead to spectacular phenomena like landslides.<sup>9,12</sup> The goal of this study is to

Department of Chemical Engineering, University of Pittsburgh, Pittsburgh, PA 15261, USA. E-mail: velankar@pitt.edu

† Electronic supplementary information (ESI) available. See DOI: 10.1039/c4sm02053g

examine physical gelation and the morphological transitions involved in ternary fluid–fluid–particle systems.

Capillary interactions have played a central role in industrial processes, such as spherical agglomeration<sup>14</sup> and wet granulation,<sup>15</sup> for several decades. Lately, capillary forces have contributed to the development of modern processes such as the design of complex folding patterns,<sup>16</sup> the assembly of nanoparticles into colloidal molecules *via* capillary condensation<sup>17,18</sup> or the formation of thermal underfills in microelectronics,<sup>19</sup> and in the field of nanolithography.<sup>20</sup> Understanding how capillary forces can be used to tune the microstructure and flow properties of fluid–fluid–particle three-phase systems is of great practical interest,<sup>21</sup> yet such knowledge relies on the complex interplay between formulation, processing and interfacial phenomena. Indeed, the interfacial phenomena in fluid–fluid–particle ternary systems have been heavily studied in the case of partially wetting particles since the emergence of Ramsden–Pickering emulsions,<sup>22,23</sup> where particles exhibit a surfactant-like effect by crowding at the fluid–fluid interface, and thus can lead to the stabilization of the emulsion morphology due to severely restricted coalescence.<sup>24–29</sup> In addition, recent research has explored the formation of percolated structures and clustering in such systems,<sup>29,30</sup> revealing that emulsion drops can assemble into a sample-spanning network due to their bridging by the particle monolayer present at the fluid–fluid interface (*Pickering gels*). Stable bicontinuous structures, resulting from arrested spinodal decomposition and dubbed bicontinuous interfacially jammed emulsion gels<sup>31–34</sup> (*bijels*), constitute another example of the rich structural possibilities of fluid–fluid–particle ternary systems.

All the abovementioned cases require that the particles should be partially-wetted by both the fluids. In contrast, here we consider situations in which the particles are almost fully wetted by one of the fluid phases. We examine the importance of ternary blend composition on the resulting microstructure and rheological properties by exploring a broad region of the compositional space. More specifically, we investigate the influence of the minority fluid phase content on capillary interactions between the solid particles, and how strong gels can be formed for a broad range of particle volume fractions in the case of *pendular* structures, *i.e.* when particles are bridged by small capillary menisci. For this investigation, we employ a pair of immiscible polymers as the two liquid phases and solid spherical particles as the third phase. The continuous polymer phase is a viscous fluid and the minority phase is a semi-crystalline solid at room temperature with a melting point around 60 °C. The ternary blends are prepared by melt mixing using a small-scale device. Importantly, we focus on the situation where the particles are almost fully wetted by the minority fluid phase. Therefore, we refer to the latter as the *wetting phase*, which can be easily solidified by cooling. This approach permits the preservation of the native aggregated structure by quenching the samples for *ex situ* characterizations. Notably, the solid aggregates can be extracted from the continuous liquid polymer phase by selective dissolution, which allows morphological observations to be performed using electron microscopy, without resorting to a cryogenic or vitrification chamber.

Capillary-induced aggregation phenomena can thus be characterized at several length scales *via* optical and electron microscopy. Using this approach, we can establish a microstructural basis for the various rheological transitions observed.

In parallel, the flow properties are examined under molten conditions using rotational rheometry. In particular, we investigate the linear and nonlinear viscoelastic behavior of capillary-bridged particle network systems, which are denoted as *pendular gels*, for a particle volume fraction that ranges from the dilute to the concentrated regime. Such a scenario is particularly relevant when the typical particle size widely exceeds that of the dispersed wetting phase, where the high wettability of the particles by the wetting phase promotes strong capillary attraction.<sup>4,5</sup> Like many attractively-driven soft materials, the microstructure of *pendular gels* features a volume-spanning backbone, which leads to a yield stress behavior. Unlike the case of concentrated systems, such as hard particle pastes<sup>35</sup> or jammed emulsions,<sup>36,37</sup> these solid-like properties arise at low particle volume fractions due to a low percolation threshold. Regardless of the nature of the components (*i.e.*, soft or hard), the solid–fluid transition observed in these systems is driven by the interactions between their components, where the particle volume fraction highly contributes to structural jamming.<sup>2,38</sup> Despite the complex pathway to a steady state flow, we find that the yielding transition observed under steady state conditions permits simple rescaling of the flow curves by taking into account the effect of volume fraction using relevant physical parameters. Similar scaling approaches have proven successful for other yielding soft materials systems like clay–water suspensions,<sup>39,40</sup> and more recently for concentrated emulsions and microgel pastes.<sup>41,42</sup>

Our study addresses the flow–structure relationships in ternary systems presenting strong capillary attraction. We focus on identifying the relevant parameters controlling the yield stress for this recent class of soft materials, and we build a state diagram based on thorough investigations on the wetting phase and particle concentration dependence. In parallel, we report on the morphological transitions due to changes in ternary composition and show for the first time that hierarchical aggregation is present in these ternary systems for some regions of compositional space.

## 2. Experimental section

### 2.1 Materials

Polyisobutylene (PIB,  $\rho \approx 0.908 \text{ g mL}^{-1}$ ,  $\bar{M}_w \approx 2200 \text{ g mol}^{-1}$ ) was purchased from Soltex and used as the continuous phase. Polyethylene oxide (PEO,  $\rho \approx 1.1 \text{ g mL}^{-1}$ ,  $\bar{M}_w \approx 20\,000 \text{ g mol}^{-1}$ , melting point  $\approx 60 \text{ °C}$ ) was purchased from Fluka and used as the minority wetting phase. Both polymers are Newtonian viscous fluids with a weak viscosity mismatch ( $\eta_{0\text{-PEO}}/\eta_{0\text{-PIB}} \approx 1.6$  at 80 °C). Fluorescein sodium salt (F63377 from Sigma Aldrich) was dissolved in PEO for confocal imaging, following a procedure described elsewhere.<sup>5</sup> Spherical silica particles (SP) with a unimodal size distribution (average diameter of 2  $\mu\text{m}$ ) were purchased from Industrial Powders under the reference SS1205.

## 2.2 Sample preparation

Blends were prepared using a mini-mixer, which is designed similarly to a Minimax cup and rotor mixer.<sup>5,29,43</sup> Briefly, the rotation of the top plate induces a Couette flow, while the addition of three brass spheres in the mixer gap improves the dispersive and distributive mixing qualities due to the associated secondary flows.<sup>43</sup> For PIB-PEO-SP ternary blends, a two-step procedure was followed. First, the PEO phase was dispersed in PIB at a rotational speed of 1200 rpm for 2 min, which leads to drop sizes close to the SP sizes. Then, SP were added and the three components were mixed together at 1000 rpm for 5 min. These two mixing steps were always performed at 80 °C to ensure that the PEO phase was in the melt state. This approach was specifically designed to prevent the poor dispersion of the PEO phase, which would eventually lead to partial compact capillary aggregation as detailed in a previous study.<sup>5</sup> Ternary blends were sealed in plastic bottles with Parafilm and cooled to 5 °C for 30 minutes to rapidly solidify the PEO phase. Binary PIB-SP blends, used for comparison, were prepared in a single mixing step at 1000 rpm for 5 min at room temperature. For each batch, the amount of recoverable material at the end of the mixing process was approximately 4 g. All the blends were placed under vacuum overnight to remove the air bubbles that were entrapped in the bulk material during the mixing process. The compositions of the ternary blends studied here are detailed in Table 1 and represented on a ternary diagram in Fig. 1. A similar range of SP volume fraction was explored for the binary PIB-SP blends. In addition, some ternary blends were prepared with fluorescent PEO for confocal microscopy; the presence of a fluorophore in the PEO phase was not found to alter the structure and rheology of the blends.

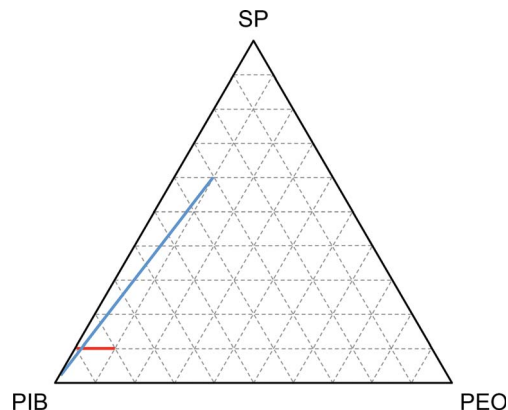


Fig. 1 Ternary composition diagram of the experimental system investigated. Red line represents the influence of the PEO content (dilute regime) for a fixed SP volume fraction ( $\phi_{SP} = 0.1$ ). Blue line corresponds to a wide variation in SP content for a fixed PEO-to-SP volume fraction ratio ( $q = \phi_{PEO}/\phi_{SP} = 0.16$ ).

## 2.3 Confocal microscopy

The blend morphology was observed with an Olympus Fluoview 1000 inverted confocal laser scanning microscope (CLSM), using a 40 $\times$  (NA = 1.30) and a 100 $\times$  (NA = 1.35) oil-immersion objectives. Micrographs were acquired in both the fluorescence and differential interference contrast (DIC) imaging modes.

## 2.4 Electron microscopy

Aggregate structures formed by the silica particles and polyethylene oxide were observed over a wide range of length scales using electron microscopy, including higher magnification details at the particles/capillary bridges scales that cannot be resolved by optical microscopy. Small quantities of the ternary blends were transferred into sample vials and subsequently immersed in *n*-octane for at least 24 hours to dissolve the PIB matrix. The resulting solid sediment, composed of silica particles and crystallized PEO, was then placed on a filter paper (Millipore, 0.1  $\mu$ m pore size) using a pipette and washed with *n*-octane. The extracted sample was left to dry and placed on a carbon-taped SEM stub, followed by metal coating using a Au/Pd sputtering target (Cresington) for 90 s at 40 mA. Morphological observations were carried out with a Philips XL30 field emission gun scanning electron microscope (FEG SEM) using a secondary electron detector. In addition, the extracted samples were placed on a formvar/carbon coated 200 mesh copper TEM grid (Ted Pella) and observed with a JEOL JEM-2100F high-resolution transmission electron microscope (HR-TEM) in the bright field mode.

## 2.5 Rheology

Rheological experiments were carried out using a TA Instruments AR-2000 stress-controlled rheometer featuring an air convection oven that ensures homogeneous sample temperature. All the experiments were conducted at 80 °C to ensure that both the polymers were in the melt-state. The ternary systems investigated here tend to exhibit significant wall slip under large shear deformations when a smooth geometry is used, as

Table 1 Compositions of the ternary blends

Blend	$\phi_{PIB}$	$\phi_{PEO}$	$\phi_{SP}$	$q = \phi_{PEO}/\phi_{SP}$
<b>Influence of PEO concentration (red line in Fig. 1)</b>				
90/0/10	0.9	0	0.1	0
89.84/0.16/10	0.8984	0.0016	0.1	0.016
89.75/0.25/10	0.8975	0.0025	0.1	0.025
89.6/0.4/10	0.896	0.004	0.1	0.04
89.37/0.63/10	0.8937	0.0063	0.1	0.063
89/1/10	0.89	0.01	0.1	0.1
88.4/1.6/10	0.884	0.016	0.1	0.16
87.5/2.5/10	0.875	0.025	0.1	0.25
86/4/10	0.86	0.04	0.1	0.4
83.7/6.3/10	0.837	0.063	0.1	0.63
80/10/10	0.8	0.1	0.1	1
<b>Influence of SP concentration (blue line in Fig. 1)</b>				
98.84/0.16/1	0.9884	0.0016	0.01	0.16
97.45/0.35/2.2	0.97448	0.00352	0.022	0.16
94.66/0.74/4.6	0.94664	0.00736	0.046	0.16
84.92/2.08/13	0.8492	0.0208	0.13	0.16
81.44/2.56/16	0.8144	0.0256	0.16	0.16
76.8/3.2/20	0.768	0.032	0.2	0.16
71/4/25	0.71	0.04	0.25	0.16
65.2/4.8/30	0.652	0.048	0.3	0.16
59.4/5.6/35	0.594	0.056	0.35	0.16
53.6/6.4/40	0.536	0.064	0.4	0.16

detailed in a previous study on similar systems.<sup>5</sup> Custom-made serrated parallel plates (25 mm diameter, 500  $\mu\text{m}$  roughness) were thus used to impose rough boundary conditions and prevent wall slip effects.<sup>5</sup> A larger cone and plate geometry (40 mm diameter, 1° cone angle, 49  $\mu\text{m}$  cone truncation gap) with smooth surfaces was also used, only for linear measurements of low viscosity samples (*i.e.* blends with low SP volume fractions).

Dynamic shear flow properties were examined by imposing an oscillatory strain  $\gamma^* = \gamma_0 e^{i\omega t}$ , where the strain amplitude  $\gamma_0$  and the angular frequency  $\omega$  are the input parameters. The stress amplitude  $\sigma_0$  and phase angle  $\delta$  are extracted from the resulting stress waveform  $\sigma^* = \sigma_0 e^{i\omega t + \delta}$  in the harmonic regime. Oscillatory strain sweeps were performed at a constant angular frequency of  $\omega = 10 \text{ rad s}^{-1}$  to determine the linear viscoelastic domain and probe the non-linear dynamic response of the blends. Angular frequency sweeps were applied from  $10^2$  to  $10^{-1} \text{ rad s}^{-1}$  within the linear viscoelastic domain. Steady state continuous shear experiments were carried out to probe the nonlinear viscoelastic behavior of the blends, using step rates with  $\dot{\gamma}$  spanning from  $10^{-2}$  to  $10^2 \text{ s}^{-1}$ . Each step rate was maintained until the steady regime (defined as less than 3% deviation in torque for 5 minutes) was reached. Finally, the transient behavior and stress-induced yielding were explored through creep tests for the selected samples.

## 3. Results

### 3.1 Effect of wetting phase content

The addition of PEO to the PIB-SP suspension greatly affects the flow behavior, as shown by the steady-state flow curves in Fig. 2a for blends with a fixed SP volume fraction of 10%. The PEO-free blend has a nearly Newtonian behavior—viscosity varies very weakly with the shear rate or stress—whereas ternary blends exhibit strong shear thinning typical of a yield stress fluid behavior, even for a PEO volume fraction as low as 0.2%. A key point here is that the viscosity measured at low rates (or stress) varies significantly with PEO concentration, whereas it tends to converge at higher rates (or stress), *i.e.*, the yield stress depends on the PEO loading, but the high shear viscosity does not. For each ternary blend, one can estimate the yield stress as the stress at which the viscosity shows a steep decrease in Fig. 2a. For greater consistency we used the Herschel-Bulkley model to fit our data and determine the yield stress. At first, the yielding transition moves towards higher stress values when PEO concentration increases, but eventually shifts to lower stress values with a further increase in PEO concentration. This non-monotonic evolution is shown more clearly in Fig. 2b, where the yield stress is plotted as a function of PEO-to-SP volume fractions ratio  $\varrho = \phi_{\text{PEO}}/\phi_{\text{SP}}$ .

As  $\varrho$  increases from  $\sim 0.01$  to  $\sim 0.2$ , the yield stress approximately quadruples and reaches the maximum value for  $\varrho \approx 0.25$ . The yield stress varies only weakly in the range of  $0.2 \leq \varrho \leq 0.4$  and eventually drops for  $\varrho > 0.4$ . Each of these three distinct zones (rise, plateau and decay of the yield stress with increasing PEO content) is associated with a specific structure of the ternary blend, which will be described next. Interestingly, these morphological changes present strong analogies with those observed in wet granular materials.

**Pendular regime.** This regime corresponds to the increase in yield stress shown in Fig. 2b. A typical DIC micrograph for  $\varrho = 0.16$  is presented in Fig. 2c, revealing that the silica particles form a connected path throughout the sample. The three-dimensional connectivity is confirmed when scanning the neighboring planes of observation in confocal microscopy, *i.e.*, the particles observed in Fig. 2c are connected to other branches of particles belonging to the neighboring out-of-focus regions. This heterogeneous network structure results from loose particle aggregation due to the formation of PEO capillary bridges between the particles, linking them together. Due to their mesoscopic dimensions, these capillary bridges cannot be observed in great detail by optical microscopy. Fig. 3 shows an HR-TEM image of a capillary bridge holding two particles in contact, revealing a concave meniscus-shaped bridge with a contact angle  $\theta$  nearly equal to zero. Moreover, the PEO is seen to spread as a thin film (few nanometers in thickness) on a small portion of the particles surface at the extremities of the meniscus. These details confirm that the silica particles are highly wetted by PEO. This type of capillary-induced particle bridging is typical of wet granular materials and is referred to as the *pendular* state of saturation.<sup>44</sup> It is noteworthy that a pendular percolating network appears at a particle packing fraction comparable to that of wet granular gases,<sup>45</sup> *i.e.*, much lower packing fraction than that of wet granular solids. This class of network structure is observed for  $\varrho \approx 0.01$ – $0.25$  and might even be achievable at lower PEO concentrations, although we presume that a critical PEO concentration, however small, has to be exceeded to allow percolation. The structure presumably reaches full pendular bridging (*i.e.* all particles contribute to the pendular network) at the onset of the plateau. This transition will be discussed later in this paper.

**Funicular regime.** In the  $0.25 \leq \varrho \leq 0.5$  range, the yield stress shows little variation but eventually starts to drop as the PEO amount increases. Concomitantly, the PEO bridges increase in size and become detectable in optical microscopy, as can be seen from the confocal fluorescence micrograph in Fig. 2d. The particles still form a percolated network structure, as shown by the SEM image in Fig. 2g. However, closer observations at the particle length scale reveal that the particle-bridging menisci are large enough to coalesce (see Fig. 2j). The morphology is thus partially pendular-like, *i.e.* particles are connected by single menisci; however, the excess of the wetting phase leads to the coalescence of neighboring menisci, analogous to the *funicular* state of saturation of wet granular materials. We emphasize that the transition between the pendular and funicular regimes is technically adequate when the particles and menisci are monodisperse or weakly polydisperse. Here, menisci coalescence is possible in the pendular regime (at least occasionally) due to the presence of small particles and large menisci. In other words, a *purely* pendular regime might not exist for polydispersed systems, and the distinction between pendular and funicular remains somewhat qualitative.

**Compact capillary aggregation regime.** The next region is marked by a steep decrease in yield stress for  $\varrho \geq 0.5$  (Fig. 2b), where the corresponding confocal fluorescence micrographs

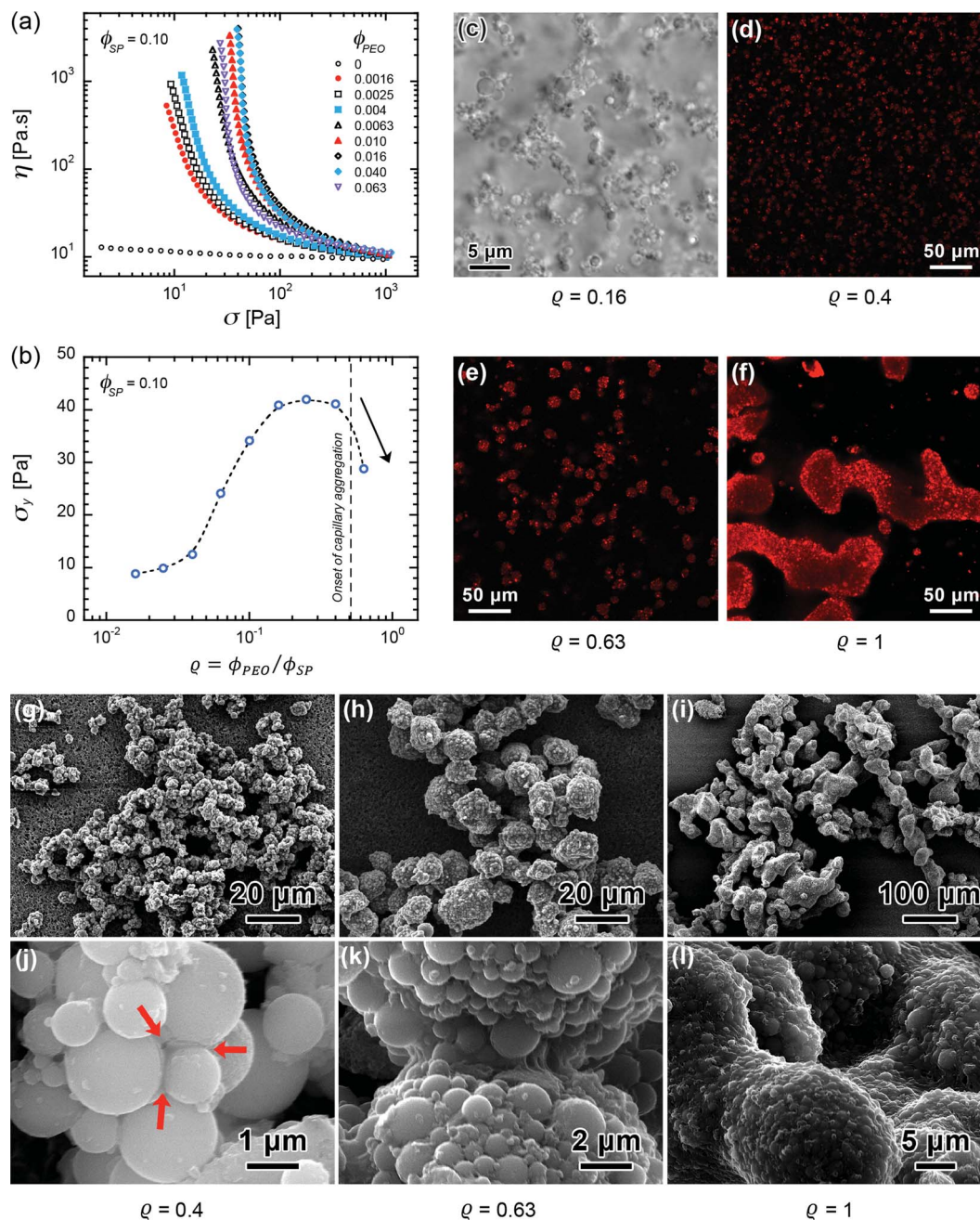


Fig. 2 Flow behavior and morphology dependence on the wetting fluid phase (PEO) content for  $\phi_{SP} = 0.10$ . (a) Steady-state flow curves (viscosity versus shear stress) showing the yield transition of the ternary systems, (b) yield stress as a function of the PEO-to-SP volume fractions ratio  $q$ . (c) DIC micrograph for  $q = 0.16$ . Fluorescent (CLSM) micrographs showing the partitioning of the PEO phase in the ternary blends: (d)  $q = 0.4$ , (e)  $q = 0.63$ , (f)  $q = 1$ . SEM observations of the SP–PEO aggregates structures after selective dissolution of the PIB matrix are shown at both the aggregate scale (upper row) and particle scale (lower row): (g and j)  $q = 0.4$ , (h and k)  $q = 0.63$ , (i and l)  $q = 1$ . Red arrows in (j) point towards the coalesced menisci holding several particles together.

(Fig. 2e and f) show that the PEO phase tends to form compact aggregates whose size drastically increase with PEO concentration. Numerous dark spots appear in the fluorescent regions of Fig. 2e and f, indicating the crowding of the non-fluorescent silica particles in the bulk PEO phase. SEM observations (Fig. 2h, i, k, l) confirm the presence of compact PEO–SP aggregates with an ellipsoid-like shape, which feature a raspberry-like morphology. Importantly, these compact aggregates

are not Pickering emulsions (*i.e.* drops with a particle-jammed surface) because the silica particles partition into the volume of the PEO phase as well as to its surface. Instead, this structure is similar to the *capillary* state of saturation in wet granular materials. We recently showed that the formation of capillary aggregates can result from particle transfer into PEO drops when the drop size widely exceeds that of the particles.<sup>5</sup> This phenomenon can occur at a much lower  $q$  than in the present

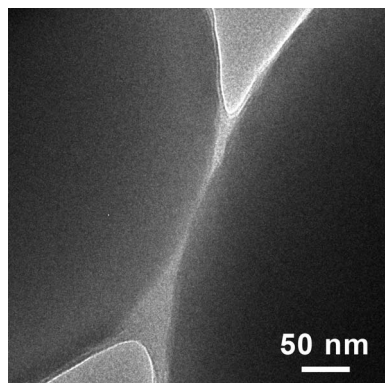


Fig. 3 HR-TEM image of a pendular gel sample ( $\phi_{SP} = 0.10$ ,  $q = 0.16$ ) showing a PEO meniscus bridging two particles. Particles diameters are 0.686  $\mu\text{m}$  (left) and 1.107  $\mu\text{m}$  (right).

situation, primarily due to the influence of the mixing procedure. Here, the two-step mixing procedure was developed specifically to impede such phenomena. Thus, the formation of compact aggregates is simply due to the large amount of the wetting phase, which leads to a complete merging of the menisci. Increasing the PEO concentration gives rise to a noticeable increase in the capillary aggregate size, from  $\sim 10$ – $20$   $\mu\text{m}$  for  $q = 0.63$  to  $\sim 20$ – $50$   $\mu\text{m}$  for  $q = 1$ . Note that the steady state flow data are omitted for  $q = 1$  because of the large fluctuations during the torque measurements, presumably due to the cluster size (see Fig. 2f), which becomes very large and starts to approach the gap size. Unexpectedly, the resulting structures do feature a three-dimensional percolating path, as shown in Fig. 2e, f, h, i, corroborating the persistence of a yield stress behavior. However, unlike in the pendular regime, networking results from the bridging of PEO-SP compact capillary aggregates (see the SEM close-up observations at the junction of the network components in Fig. 2k and l). These structures appear to result from an arrested state where compact capillary aggregates appear partially merged together to form a connected path. At a larger scale, the increase in PEO content accentuates a two-phase separation between the PIB matrix and the percolating PEO-SP aggregate through the growth of PEO-SP domains. To our knowledge, such hierarchical clustering resulting from the percolation of capillary aggregates has not been reported before.

### 3.2 Rheological shift induced by pendular bridging

So far, the addition of PEO has shown a dramatic impact on the steady-state shear flow properties, where the yield stress is maximum in the pendular state. In this section, we expand our study to the rheological changes caused by pendular bridging through dynamic measurements in both linear and nonlinear viscoelastic domains. For this purpose, we compare the behavior of binary PIB-SP ( $q = 0$ ) and ternary PIB-PEO-SP ( $q = 0.16$ , corresponding to full pendular bridging) systems. Results are shown for  $\phi_{SP} = 0.2$  in both the cases (the influence of particle concentration will be presented in the next section).

**Linear viscoelasticity.** The elastic ( $G'$ ) and viscous ( $G''$ ) moduli measured during the frequency sweep experiments in the linear domain are plotted in Fig. 4. The binary system exhibits a liquid-like behavior ( $G'' > G'$ ) at high frequencies. However, both moduli superimpose at intermediate/low frequencies ( $0.1 \text{ rad s}^{-1} \lesssim \omega \lesssim 1 \text{ rad s}^{-1}$ ), where  $G'(\omega) \approx G''(\omega) \sim \omega^{1/2}$ . The latter relaxation mode mimics the criterion of Winter and Chambon<sup>46</sup> for determining the gel point in polymer networks. This indicates that short-range attractions between the silica particles in the PIB medium start to affect the suspension dynamics at this concentration ( $\phi_{SP} = 0.2$ ). Similar viscoelastic scaling was observed close to the physical gelation of other particle-based systems such as weakly attractive depletion colloidal gels<sup>47</sup> and thermoreversible attractive nanoparticle dispersions with short-range interactions.<sup>48</sup>

The ternary system shows an altogether different response, corresponding to a solid-like behavior.  $G'$  exhibits a very weak increase with  $\omega$  (plateau region), while  $G''$  exhibits a local minimum around  $\omega = 4 \text{ rad s}^{-1}$ , with  $G' \gg G''$  in this  $\omega$ -range. Such behavior is reminiscent of many soft materials such as colloidal gels<sup>49,50</sup> and glasses<sup>51</sup> and concentrated star polymer solutions.<sup>52</sup> Although the accessible timescale window is often limited to the plateau region, this peculiar linear viscoelastic response fits in the framework of glassy dynamics,<sup>1,53–55</sup> where the complete timescale spectrum involves two relaxation phenomena: a short time (large frequency) relaxation corresponding to limited particles motion due to neighboring hindrance ( $\beta$ -relaxation), and a long time (small frequency) relaxation involving larger collective motions ( $\alpha$ -relaxation). The plateau region observed in Fig. 4 lies in between these relaxation processes, and the local  $G''$  minimum denotes the

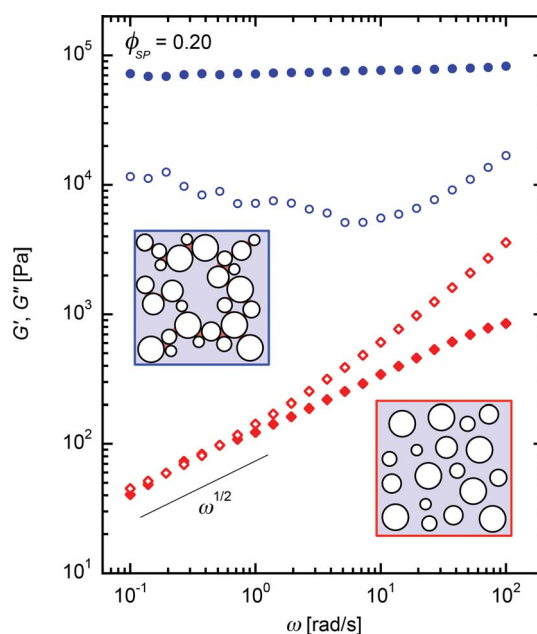


Fig. 4 Angular frequency dependence of elastic modulus  $G'$  (filled symbols) and viscous modulus  $G''$  (open symbols) in the linear viscoelastic regime for binary ( $q = 0$ , red diamonds) and ternary ( $q = 0.16$ , blue circles) systems, both at  $\phi_{SP} = 0.20$ .

transition between  $\alpha$  and  $\beta$  relaxation modes. Importantly, this solid-like behavior supports the formation of a physical gel *via* the pendular bridging of silica particles by the PEO phase, where attractive capillary forces widely exceed van der Waals interactions, leading to a significant increase in sample elasticity compared to the binary PIB-SP system.

**Nonlinear dynamic response.** The results of the oscillatory strain amplitude sweep experiments are presented in Fig. 5. A departure from the linear viscoelastic regime is observed at a very low strain amplitude for the ternary system (around  $\gamma_0 = 3 \times 10^{-4}$ ). In contrast, the linear domain of the binary system extends to higher strain amplitudes (almost a decade higher compared to the limit of linearity of the ternary system). Moreover, the binary sample exhibits strain thinning at larger strain amplitudes, which is typical of polymer melts and suspensions, with the viscous behavior dominating ( $G'' > G'$ ) across the entire range of deformation at this angular frequency ( $\omega = 10 \text{ rad s}^{-1}$ ).

In contrast, the ternary system displays a  $G'$  decay concomitantly to a  $G''$  overshoot (corresponding to a *weak strain overshoot* or *type III LAOS* behavior in the terms of Hyun *et al.*<sup>56</sup>), directly followed by a  $G'-G''$  crossover (shear-induced fluidization) and strain thinning. Such nonlinear response is a hallmark of yielding soft gels/glasses<sup>57-59</sup> and heterogeneous filled-polymers.<sup>60</sup> The local maximum in  $G''$  is related to the dissipation processes induced by the internal rearrangements of the network structure under shear strains exceeding the linear domain. It should result from a competition between the creation and the rupture of network junctions within the sample, although its interpretation may vary

because it is still a matter of debate.<sup>56</sup> From a theoretical standpoint, this type of LAOS behavior was well-described using the mode-coupling theory<sup>58,61</sup> and alternatively using a modified Leonov model taking into account the internal reorganization of the flocs.<sup>60</sup>

The strain thinning regime observed for  $0.04 \lesssim \gamma_0 \lesssim 1$  in Fig. 5 is marked by decreasing power laws of the complex moduli ( $G' \sim \gamma_0^{-\nu'}$  and  $G'' \sim \gamma_0^{-\nu''}$ ). The thinning trend is more pronounced in the case of the ternary system, as indicated by the larger values of the exponents  $\nu'$  and  $\nu''$  compared to the binary system. We note that the values of the power law exponents for the ternary blend ( $\nu' \approx 1.3$  and  $\nu'' \approx 0.8$ ) are close to those found in other soft glassy systems,<sup>42,61</sup> where the  $\nu'/\nu''$  ratio is usually close to 2.<sup>61-64</sup> At a larger strain, a shouldering is observed for both the moduli. This phenomenon can be noticed for the binary and ternary system at a similar strain (around  $\gamma_0 = 1$ ). Similar results were found in colloidal gels<sup>49,65,66</sup> and attractive glasses,<sup>51</sup> where the inflection is regarded as a secondary yield point reflecting the restructuring of large aggregates for gels and cage breaking of colloidal particles for attractive glasses. In our investigation, we can only speculate that such behavior reflects the fracture of finite size particle flocs following the yielding of the network structure. Importantly, this is not specific to the case of pendular bridging because it is observed for both binary and ternary samples.

In addition, we must specify that a strong nonlinear viscoelastic response usually leads to distorted stress waveforms with the contribution of higher order odd harmonics,<sup>56</sup> *i.e.*, the system oscillates in the anharmonic regime. In this case, the

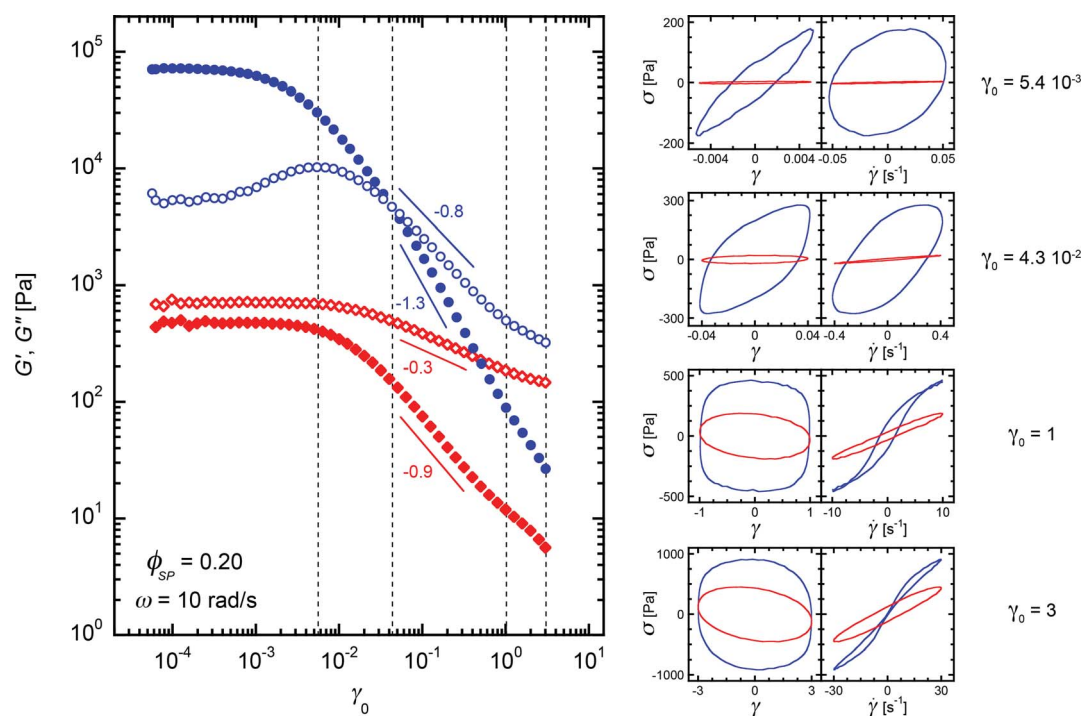


Fig. 5 Large amplitude oscillatory shear (LAOS) rheology results showing  $G'$  (filled symbols) and  $G''$  (open symbols) as a function of strain amplitude ( $\omega = 10 \text{ rad s}^{-1}$ ) for binary ( $\varrho = 0$ , red diamonds) and ternary ( $\varrho = 0.16$ , blue circles) systems, both at  $\phi_{SP} = 0.20$ . Moduli values in the non-linear regime correspond to the first harmonic approximation. The elastic ( $\sigma$  vs.  $\gamma$ ) and viscous ( $\sigma$  vs.  $\dot{\gamma}$ ) Lissajous-Bowditch curves for the strain amplitudes marked by dashed lines are shown on the right panel.

$G'(\gamma_0)$  and  $G''(\gamma_0)$  data extracted from the rheometer software correspond to the apparent moduli in the first harmonic approximation and do not consider the anharmonic response. Further analysis, like parametric plots of stress *vs.* strain and strain rate (Lissajous–Bowditch curves) or Fourier transform of the stress waveforms,<sup>56</sup> is then required to probe the nonlinear behavior. We compare the Lissajous–Bowditch curves for the binary and ternary systems at four levels of  $\gamma_0$  in the nonlinear domain on Fig. 5 (the selected  $\gamma_0$  values are indicated by the dashed lines in the strain sweeps graph). The binary system shows elliptical shapes regardless of the strain amplitude, indicating that the nonlinear viscoelastic response remains in the harmonic regime all along the strain sweep. However, the ternary system already shows deviation from the harmonic response at the peak of the  $G''$  overshoot. This trend accentuates at the  $G'-G''$  crossover and leads to strong higher odd harmonics contribution after the fluidization of the system (at  $\gamma_0 = 1$  and 3), marked by an increasingly rectangular shape for  $\sigma$  *vs.*  $\gamma$  (elastic Lissajous–Bowditch curve) and accompanied by an S-shape in the  $\sigma$  *vs.*  $\dot{\gamma}$  plot (viscous Lissajous–Bowditch curve) due to plastic events<sup>62</sup> (presumably rearrangements of the gel structure). Similar in-cycle anharmonic responses are observed in associative polymer gels,<sup>56</sup> concentrated solutions of soft star-like micelles<sup>64</sup> and depletion colloidal gels.<sup>67</sup>

Finally, the yielding of the pendular network structure can also be inferred from the oscillatory strain–stress amplitudes plot, where the elastic to plastic transition coincides with the fluidization point ( $G'-G''$  crossover), which can be used to define the yield stress (see ESI Fig. S1†).

### 3.3 Particle concentration dependence and scaling properties in the pendular regime

Pendular ternary systems were prepared across a wide range of particle concentrations with a fixed PEO–SP volume ratio  $\varrho = 0.16$ , which was selected to ensure full pendular bridging based on the results obtained at  $\phi_{\text{SP}} = 0.1$  (see Fig. 2b). Note that a higher value of  $\varrho$  up to 0.25 would yield almost identical results in terms of structure and rheological behavior, but could potentially lead to a partial merging of the menisci as both  $\phi_{\text{PEO}}$  and  $\phi_{\text{SP}}$  increase. The ternary system thus moves along the blue line of the compositional space, as shown in Fig. 1.

The optical images of the ternary samples for  $\phi_{\text{SP}}$  between 0.01 and 0.25 are presented in ESI Fig. S2.† At low volume fractions (namely,  $\phi_{\text{SP}} = 0.01$  and 0.022), no volume-spanning structure is formed, yet we observe the presence of particle flocs due to pendular bridging, with a characteristic size of approximately 10 to 20  $\mu\text{m}$ . The increase in particle concentration leads to a three-dimensional connectivity of the flocs. At  $\phi_{\text{SP}} = 0.046$ , the flocs grow into a pendular network, suggesting a percolation threshold slightly below this value. A further increase in  $\phi_{\text{SP}}$  results in a higher network density, while sustaining an open branched structure. However, a more compact macroporous structure appears at  $\phi_{\text{SP}} \geq 0.35$ , with larger scale heterogeneity resulting from the coexistence of particle-rich and particle-poor regions. This is shown in Fig. 6 for  $\phi_{\text{SP}} = 0.40$ , where the particle-poor regions become as large

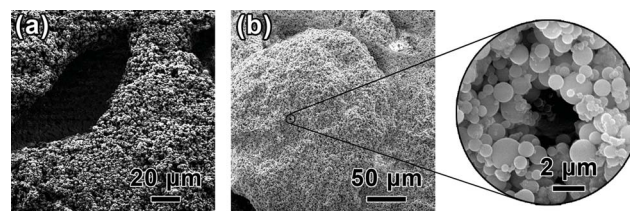


Fig. 6 SEM pictures of PEO–SP macroporous structure obtained in a pendular gel at high particle concentration ( $\phi_{\text{SP}} = 0.40$ ,  $\varrho = 0.16$ ) showing large scale heterogeneity. The void regions left after removal of the PIB appear clearly in (a). The compact particle-rich region is shown at a lower magnification in (b), with a magnified view highlighting the pendular morphology. (a) and (b) represent different portions of the same sample.

as 100  $\mu\text{m}$ . We emphasize that the SP–PEO structure is not saturated with PEO and remains pendular-like, as can be seen in the magnified view of Fig. 6b.

**Scaling of linear viscoelastic response.** Complex moduli and viscosity measured during frequency sweeps are represented in Fig. 7a and b respectively. Note that these measurements were carried out in a  $\phi_{\text{SP}}$  range where the pendular percolating network structure is well established ( $\phi_{\text{SP}} > 0.10$ ). For  $\phi_{\text{SP}} < 0.10$ , the low viscosities of the samples fall into the resolution limits

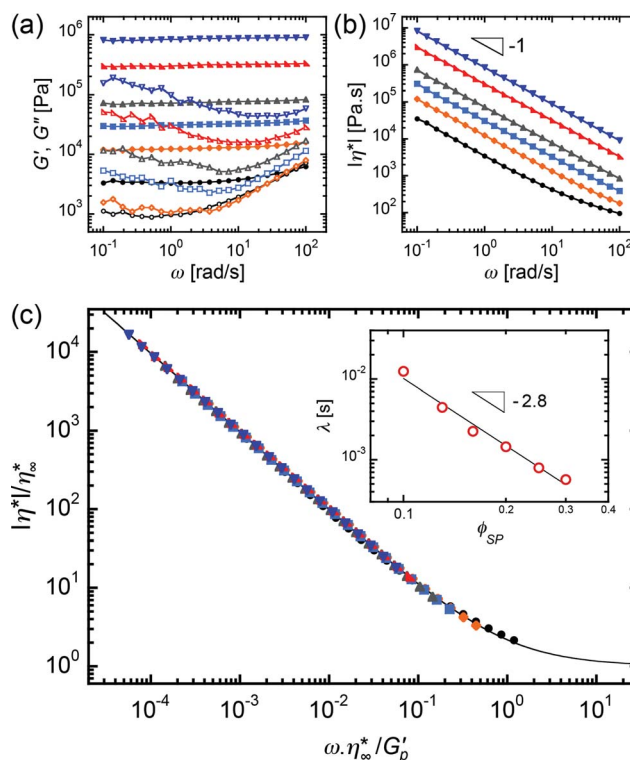


Fig. 7 Linear viscoelasticity of the ternary systems: (a)  $G'$  (closed symbols) and  $G''$  (open symbols), (b) magnitude of the complex viscosity  $|\eta^*|$  *vs.* angular frequency for  $\phi_{\text{SP}} = 0.10$  (black circles), 0.13 (orange diamonds), 0.16 (blue squares), 0.20 (grey triangles), 0.25 (red tilted triangles) and 0.30 (blue inverted triangles), all for  $\varrho = 0.16$ . (c) Dimensionless plot for the scaling of the linear viscoelastic response (continuous line represents the best fit using eqn (1)). Inset shows the characteristic time  $\lambda = \eta_{\infty}^*/G_p'$  *vs.*  $\phi_{\text{SP}}$ .

of the instrument at low/moderate frequencies. The  $G'(\omega)$ - $G''(\omega)$  spectra are similar to those previously presented for the ternary system in Fig. 4. The increase in  $\phi_{\text{SP}}$  clearly leads to higher  $G'$ ,  $G''$  and  $|\eta^*|$  values over the entire  $\omega$ -range, while the local  $G''$  minimum, as well as the  $G'-G''$  crossover, is shifted towards higher  $\omega$ . Notably, the magnitude of the complex viscosity decreases as  $\omega^{-1}$  until it tends towards a plateau value  $\eta_\infty^*$  at high frequencies. The transition between these two regimes corresponds to the high frequency  $G'-G''$  crossover, which occurs at the angular frequency  $\omega_c = 1/\lambda$ , where the characteristic time  $\lambda = \eta_\infty^*/G'_p$  is associated with the  $\beta$ -relaxation (see ESI†).

Because a similar linear viscoelastic behavior is observed for the pendular gels for a wide range of  $\phi_{\text{SP}}$ , we show that the data obtained at various  $\phi_{\text{SP}}$  can be scaled using only two physical parameters:  $\lambda$  and  $G'_p$ . We define the dimensionless angular frequency as  $\tilde{\omega} = \eta_\infty^*\omega/G'_p$  and the dimensionless magnitude of the complex viscosity as  $\tilde{\eta}^* = |\eta^*|/\eta_\infty^*$ . The elastic modulus at the plateau  $G'_p$  is defined as the average value of  $G'$  over the  $\omega$ -range where the plateau is observed. However, the viscosity plateau  $\eta_\infty^*$  cannot always be directly measured, especially for higher  $\phi_{\text{SP}}$  values, where the viscosity plateau shifts towards high frequencies that are experimentally out of reach. Nevertheless, we presume that such a high frequency plateau must exist as the rheology becomes dominated by the viscous contribution of the components. Accordingly,  $\eta_\infty^*$  (and therefore  $\lambda$ ) was used as an adjusting parameter to realize the best overlap of  $\tilde{\eta}^*$  vs.  $\tilde{\omega}$ . The dimensionless graph  $|\eta^*|/\eta_\infty^*$  vs.  $\eta_\infty^*\omega/G'_p$  is displayed in Fig. 7c. All the data points collapse on a single curve, suggesting that the viscoelastic properties can, to a first approximation, be captured by the network modulus  $G'_p$  and a single characteristic time  $\lambda$ . This characteristic time is found to scale as  $\phi_{\text{SP}}^{-2.8}$  (the dependence of  $G'_p$  on particle volume fraction will be discussed later). The following empirical constitutive equation can describe this linear viscoelastic behavior:

$$\tilde{\eta}^* = 1 + k(\tilde{\omega})^{-1/2} + (\tilde{\omega})^{-1} \quad (1)$$

with  $k = 0.22$ .

However, when this simple scaling argument is applied to  $G'$  and  $G''$  using their dimensionless counterparts ( $\tilde{G}' = G'/G'_p$  and  $\tilde{G}'' = G''/G'_p$ , respectively), a good agreement is still found for the scaling of  $G'$ , but the  $G''$  data do not superimpose adequately (see ESI Fig. S6†). In particular,  $\tilde{G}''$  appears much closer to  $\tilde{G}'$  for the lowest particle concentration examined ( $\phi_{\text{SP}} = 0.10$ ) than for the higher concentrations. It should be noted that the horizontal scaling brings all the local  $G''$  minima to the same value of  $\tilde{\omega}$ , confirming that the single timescale approach (using  $\lambda$ ) works well for our system. Such discrepancies in the vertical scaling of  $G''$  suggest that the dissipation processes depend on  $\phi_{\text{SP}}$  in a more intricate way than elastic properties.

Alternatively, we also attempted to use the scaling approach developed by Trappe and Weitz<sup>38</sup> for weakly attractive particles, where a master curve can be obtained using horizontal (for  $\omega$ ) and vertical (for  $G'$  and  $G''$ ) shift factors. Because both the shift factors can be arbitrarily chosen, we find that the superposition of  $G''$  can be slightly enhanced, but this also results in a poorer superimposition of the  $G'$  data and a disparity in the position of the local  $G''$  minimum (see ESI Fig. S7†). Overall, this approach

does not provide a better scaling of the linear viscoelasticity of the pendular gels.

**Scaling of steady state shear flow behavior.** The flow curves in the steady state regime are shown in Fig. 8a. A nearly Newtonian behavior ( $\sigma(\dot{\gamma}) = \eta_0\dot{\gamma}$ ) is observed for the lower  $\phi_{\text{SP}}$  values, while a stress plateau develops at low shear rates when  $\phi_{\text{SP}} \geq 0.046$ . This confirms the existence of a percolation threshold  $\phi_{\text{per}} \approx 0.04$  that marks a transition towards the formation of a three-dimensional stress bearing pendular network structure for  $\phi_{\text{SP}} > \phi_{\text{per}}$ , in agreement with direct observations (Fig. S2†). Below the threshold, a non-Newtonian region marked by a succession of shear thickening and shear thinning at a low shear rate is observed (detailed in ESI†); however, no yield stress can be detected.

In contrast, the system shows a Herschel-Bulkley behavior<sup>68</sup> above the percolation threshold. The asymptotic stress value at low shear rates corresponds to the yield stress  $\sigma_y$ , whereas a Newtonian flow regime is eventually reached at higher shear rates. The transition between these two regimes is marked by a critical shear rate value  $\dot{\gamma}_c$ . For  $\dot{\gamma} < \dot{\gamma}_c$ , the weak increase in stress in the plateau region reflects slow rearrangements of the network structure, whereas the Newtonian behavior observed for  $\dot{\gamma} \gg \dot{\gamma}_c$  corresponds to the flow of the fragmented gel, which is associated with the viscosity  $\eta_\infty$  measured at high shear rates.

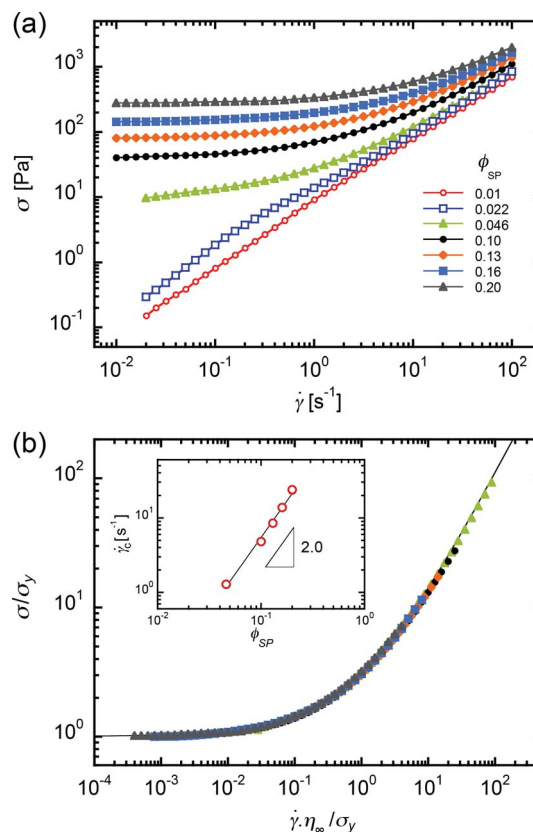


Fig. 8 (a) Steady state flow curves of the ternary systems at various  $\phi_{\text{SP}}$ , all for  $q = 0.16$ . (b) Dimensionless plot of the same data for  $\phi_{\text{SP}} \geq 0.046$  (continuous line represents eqn (2)). Inset shows the critical shear rate  $\dot{\gamma}_c = \sigma_y/\eta_\infty$  vs.  $\phi_{\text{SP}}$ .

Inspired by the approach of Coussot for attractive clay suspensions,<sup>39</sup> we surmise that the yielding transition is driven by only two parameters, namely  $\sigma_y$  and  $\dot{\gamma}_c$ . We can define the critical shear rate as  $\dot{\gamma}_c = \sigma_y/\eta_\infty$  (see ESI Fig. S4† and the corresponding discussion). The dimensionless stress  $\bar{\sigma} = \sigma/\sigma_y$  is plotted as a function of the dimensionless shear rate  $\tilde{\gamma} = \eta_\infty \dot{\gamma}/\sigma_y$  in Fig. 8b, where all the data appear to superimpose well. As shown in the inset, the critical shear rate increases with the particle volume fraction ( $\dot{\gamma}_c \sim \phi_{SP}^2$ ), indicating that the yielding transition occurs at higher rates when the network density increases. When  $\tilde{\gamma} \ll 1$ ,  $\bar{\sigma}$  tends to 1, whereas  $\bar{\sigma} = \tilde{\gamma}$  for  $\tilde{\gamma} \gg 1$ . The overall behavior is captured by the following empirical constitutive equation:

$$\bar{\sigma} = 1 + (\tilde{\gamma})^{1/2} + \tilde{\gamma} \quad (2)$$

where no adjustment parameter is needed. It is noteworthy that  $\eta_\infty$  could not always be precisely evaluated from the flow curves because very high shear rates could not be probed in practice by rotational rheometry. Some adjustment of the  $\eta_\infty$  value was

thus required to scale the data in Fig. 8b, especially at high  $\phi_{SP}$ . However, the consistency of the adjusted values was tested through the dependence of  $\eta_\infty$  on  $\phi_{SP}$ . The hydrodynamic function  $\psi(\phi_{SP})$ , defined as  $\eta_\infty(\phi_{SP}) = \psi(\phi_{SP})\eta_\infty(0)$  where  $\eta_\infty(0)$  is simply the Newtonian viscosity of the continuous phase is represented in Fig. 9. The data were fitted with the Quemada model:<sup>69</sup>

$$\psi(\phi_{SP}) = \left(1 - \frac{\phi_{SP}}{\phi_M}\right)^{-2} \quad (3)$$

where  $\phi_M$  is the maximum packing fraction. The best fit is obtained for  $\phi_M \approx 0.67$  (see continuous line in Fig. 9), which is suitable for polydisperse spheres.<sup>70,71</sup> Furthermore, the data were compared to those obtained for the binary PIB-SP system, where  $\eta_\infty$  is experimentally accessible. The differences between the binary and ternary systems are not significant (Fig. 9). This confirms that for the ternary systems, the high shear rate viscosity,  $\eta_\infty$ , is equivalent to the viscosity of the suspension without capillary interactions.<sup>5</sup>

**Yielding under LAOS.** The results of the strain sweep experiments for  $\phi_{SP} = 0.10$ – $0.30$  are presented in Fig. 10. Equivalent experiments for PIB-SP binary samples are presented in ESI (see Fig. S3b†). Increasing  $\phi_{SP}$  leads to a reduction of the linear viscoelastic domain. Similar phenomena have been widely reported for polymer nanocomposites<sup>72</sup> and colloidal gels.<sup>51,73</sup> Simultaneously, the strain associated to the peak in  $G''$  decreases when  $\phi_{SP}$  increases. It should be noted that no  $G''$  overshoot can be detected for  $\phi_{SP} = 0.10$ , as opposed to the case of higher  $\phi_{SP}$  samples. This further corroborates the difference in the dissipative process for lower  $\phi_{SP}$  pendular gels. In addition, the limit of linearity appears sensitive to  $\phi_{SP}$ , while the shouldering observed at large strains shows almost no dependence on the volume fraction of the particles (see ESI, Fig. S8†).

The LAOS results allow three strain values to be defined: the critical strain  $\gamma_{crit}$  (which marks the limit of linearity, *i.e.* the strain below which  $G'$  and  $G''$  are strain-independent, as judged

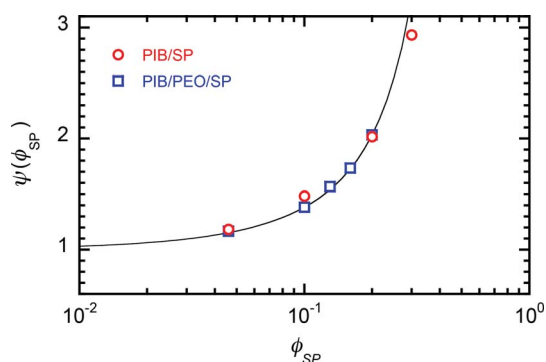


Fig. 9 Hydrodynamic function for the binary PIB-SP ( $\phi = 0$ , red circles) and ternary PIB-PEO-SP ( $\phi = 0.16$ , blue squares) systems. Continuous line represents the best fit using eqn (3).

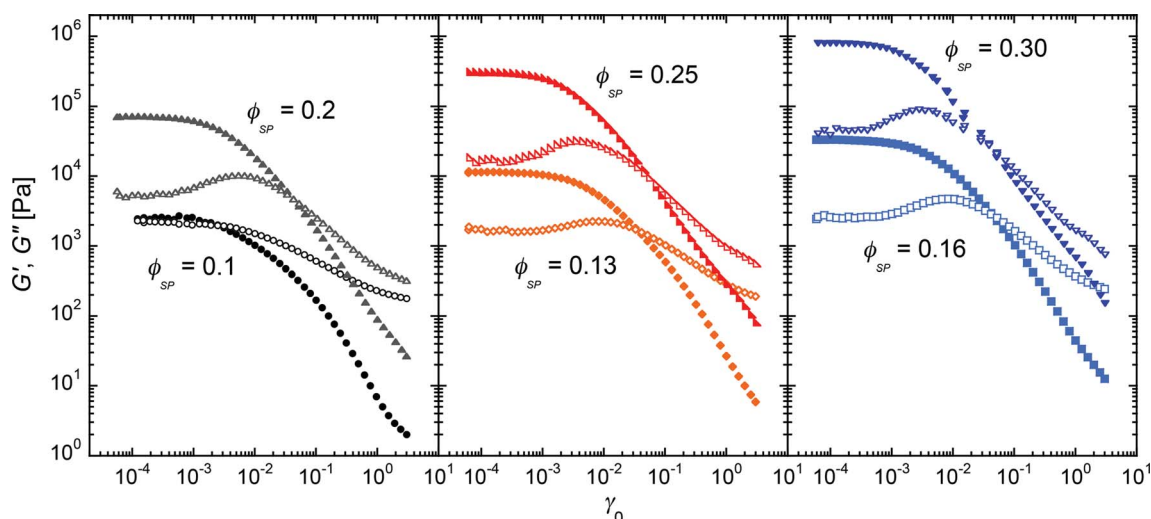


Fig. 10 LAOS behavior for the ternary systems at various  $\phi_{SP}$ , all for  $\phi = 0.16$ :  $G'$  (filled symbols) and  $G''$  (open symbols) as a function of strain amplitude ( $\omega = 10 \text{ rad s}^{-1}$ ). The results are split in three graphs to enhance clarity. Analogous data for the binary system are shown in ESI Fig. S3b.†

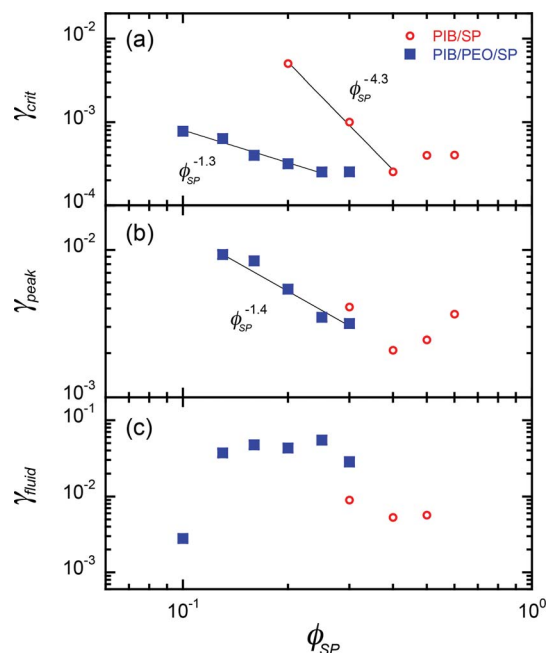


Fig. 11 Characteristic strains as a function of particle volume fraction for the binary ( $g = 0$ , red circles) and ternary ( $g = 0.16$ , blue squares) systems: (a)  $\gamma_{\text{crit}}$ , (b)  $\gamma_{\text{peak}}$  and (c)  $\gamma_{\text{fluid}}$ .

visually), the strain at the  $G''$  maximum  $\gamma_{\text{peak}}$ , and the strain at the fluidization point  $\gamma_{\text{fluid}}$  (defined at the  $G' - G''$  crossover). The evolution of all three strains as a function of  $\phi_{\text{SP}}$  are reported and compared to the results obtained for the PIB-SP binary samples in Fig. 11. The strongest impact of pendular bridging is observed on  $\gamma_{\text{crit}}$ , for which a significant reduction is found for the ternary system in comparison with the binary system at a fixed  $\phi_{\text{SP}}$  value up to approximately 0.4. In this region, the limit of linearity decreases as a power law  $\gamma_{\text{crit}} \sim \phi_{\text{SP}}^{-\varepsilon}$  with an exponent  $\varepsilon$  of 4.3 for the binary system and 1.3 in the case of the ternary system. The trend of  $\gamma_{\text{crit}}$  is less clear at higher  $\phi_{\text{SP}}$  values, but appears to saturate around  $\gamma_{\text{crit}} \approx 2\text{--}4 \times 10^{-4}$ , which can be attributed to a  $\phi_{\text{SP}}$  range approaching the glass transition for near hard spheres. It must be noted that while Fig. 11 plots the results for the binary and ternary systems on the same graphs for comparison, there is in fact almost no overlap in the  $\phi_{\text{SP}}$  range in which  $\gamma_{\text{peak}}$  and  $\gamma_{\text{fluid}}$  can be measured.

Strain thinning and yielding of the ternary samples under LAOS conditions should rely on menisci elongation and menisci rupture, respectively. The pairwise interaction due to a pendular bridge between spherical particles has been widely investigated and is known to induce an attractive force, which decreases as the particles separation distance increases<sup>74,75</sup> until the meniscus breaks. This decrease in strength could explain the strain thinning observed at very low strain amplitudes because the sharpest decrease in attractive force is observed as the particles start to separate from each other.<sup>74,75</sup> The onset of nonlinearities is also strongly coupled to the branched structure of the pendular network, which can deform heterogeneously and limit particle separation. As a result, the shortening of the linear viscoelastic domain, which is associated with the

increase of  $\phi_{\text{SP}}$ , can be understood as the restrained ability of the structure to accommodate the deformation due to the increase in the network density. In addition, when two successive strain sweeps (with an identical strain amplitude range as in Fig. 10) are applied to a pendular gel, the linear viscoelastic moduli measured during the second sweep are lower compared to those found during the first sweep (results not shown here), showing that irreversible yielding occurs during the strain sweeps. Such microstructural changes may be induced when particle separation exceeds the meniscus breaking point, which depends on the meniscus volume.<sup>74</sup> We note that meniscus or particle polydispersity may play a key role, *e.g.*, menisci with smaller volumes are expected to break at a low strain. However, as long as the meniscus does not break, the attractive force tends to bring back the particles in contact when the mechanical load is released. This “capillary recoil” suggests that the interruption of the nonlinear dynamic shear flow prior to the yield strain would result in a rheological reset of the pendular gels due to their structural recovery.

**Transient behavior under creep: delayed yielding.** When subjected to creep (*i.e.* constant stress), yield stress fluids exhibit two distinct regimes: below a critical stress, their viscosity becomes extremely large with time (the shear rate tends to zero), while at higher stresses their viscosities decrease with time and eventually reach a steady state (the shear rate increases and levels off), a phenomenon known as *viscosity bifurcation*.<sup>76,77</sup> If the applied stress is in the vicinity of the critical stress, the transient creep behavior can give way to the fluidization of the system after a long period of time. Such behavior is referred to as *delayed yielding*<sup>78,79</sup> and is observed in pastes,<sup>80,81</sup> colloidal gels<sup>78–85</sup> and glasses.<sup>86</sup>

This scenario was tested for pendular gels. The evolutions of  $\gamma$  and  $\dot{\gamma}$  in time for several values of  $\sigma$  are shown in Fig. 12a and b for a pendular sample with  $\phi_{\text{SP}} = 0.2$ . The overall transient response towards the steady state involves five main phases, although all of the phases may not be observable within the experimental time-window at all stresses. At first, an elastic response is observed shortly after the start-up of the experiment ( $t < 0.02$  s), followed by the power law decrease of the shear rate with time (usually referred to as *primary creep*<sup>85,87</sup>). The end of the latter phase is marked by an overshoot in  $\dot{\gamma}(t)$ , directly followed by another power law decrease. Finally, the material undergoes terminal fluidization and exhibits a significant increase in  $\dot{\gamma}(t)$  (up to several orders of magnitude) before reaching a plateau (steady state). We note that this last increase in  $\dot{\gamma}(t)$  is not always completely monotonic.

At the lowest applied stress, the primary creep regime remains uninterrupted at the end of the experiment duration, and the associated strain exhibits a slight increase with time. Furthermore, the primary creep regime obeys the power law  $\dot{\gamma}(t) \sim t^{-0.9}$ , leading to extremely low shear rates ( $\dot{\gamma}(t) < 10^{-5} \text{ s}^{-1}$ ). This is similar to the case of colloidal gels, where the analogy to Andrade’s law for solids ( $\dot{\gamma}(t) \sim t^{-2/3}$ ) is often invoked.<sup>81,84,85</sup> As  $\sigma$  increases, the variations in  $\dot{\gamma}(t)$  become less pronounced and the fluidization process is accelerated. The final values of  $\dot{\gamma}$  are in good agreement with the steady state flow curve obtained in the rate-controlled mode, as shown in the inset of Fig. 12b,

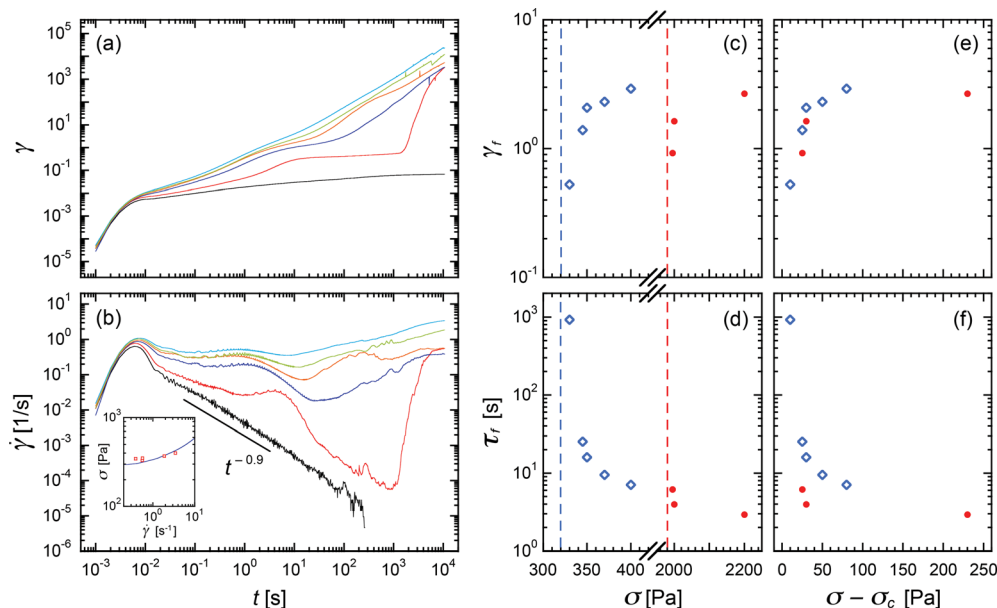


Fig. 12 Transient creep response of pendular gels. Left panel: (a) strain and (b) shear rate vs. creep time for  $\phi_{\text{SP}} = 0.20$ , with  $\sigma = 280, 330, 345, 370, 400$  Pa, from bottom to top. Inset of (b) shows the comparison of the data at the end of creep tests (red symbols) with the rate-controlled steady state flow curve (blue line). Right panel: apparent fluidization strain (c and e) and fluidization time (d and f) vs.  $\sigma$  and  $\sigma - \sigma_c$  for  $\phi_{\text{SP}} = 0.20$  (blue diamonds) and  $0.30$  (red circles). The dashed lines in (c) and (d) represent  $\sigma_c$ .

although the steady state plateau values may not be fully reached at the end of the creep test. The reason why the shear rate re-enters a power law decrease regime after the overshoot is unclear at this point. However, the two-step fluidization observed for pendular gels must involve microstructural processes, in which the rupture of capillary bridges plays a central role.

Next, the influence of  $\sigma$  on the terminal fluidization was examined through two observables: the fluidization strain  $\gamma_f$  and the fluidization time  $\tau_f$ , defined as the corresponding strain and time at the local  $\dot{\gamma}$  minimum that precedes the final increase in shear rate. Importantly, macroscopic strains measured by the rheometer prior to the steady state (such as  $\gamma_f$ ) should be regarded as *apparent* strains because the transient yielding processes are possibly localized along the gap direction. Indeed, recent studies combining rheometry and ultrasonic velocimetry have shown that the route to a steady state flow under creep conditions include several heterogeneous strain field regimes, where plug-like flow and shear banding occur around the fluidization point for yield stress fluids such as carbon black gels<sup>83,85</sup> and Carbopol microgels.<sup>84</sup> We plot  $\gamma_f$  and  $\tau_f$  as a function of the applied stress in Fig. 12c and d, respectively, for  $\phi_{\text{SP}} = 0.2$  and  $0.3$ . Similarly to other particulate gels,<sup>82</sup>  $\gamma_f$  does not appear as stress-independent. Instead, it increases sharply with the applied stress above a critical value  $\sigma_c$  and tends to level off at higher stresses. This suggests that the activated yielding dynamics during creep are sensitive to the macroscopic stress applied to the pendular gels. It is noteworthy that these fluidization strains are up to twenty-fold higher than the values found in strain-controlled LAOS experiments (compare with Fig. 11c for  $\phi_{\text{SP}} = 0.2$  and  $0.3$ ). Such

discrepancies point out the difference in the yielding scenario between strain-controlled and stress-controlled experiments, where the strain field can be highly localized at the onset of solid-fluid transition during creep tests. Moreover,  $\tau_f$  decreases significantly when  $\sigma$  starts to exceed  $\sigma_c$ , whereas a less pronounced decrease is observed at higher stresses. This dependence is reminiscent of that observed in recent studies<sup>78,79</sup> on various colloidal gels (namely carbon black gels, depletion gels and thermoreversible gels), where it is interpreted as a change in the network rupture kinetics. In addition, we find a reasonable superposition of the results obtained for  $\phi_{\text{SP}} = 0.2$  and  $0.3$  when  $\gamma_f$  and  $\tau_f$  are plotted as a function of the reduced stress  $\sigma - \sigma_c$ , as shown in Fig. 12e and f, which suggests that a similar transient creep behavior is experienced by the pendular gels when  $\sigma > \sigma_c(\phi_{\text{SP}})$ . Finally, the values obtained for  $\sigma_c$  are close to those of the yield stress  $\sigma_y$  extracted from the rate-controlled steady state flow curves and oscillatory strain sweeps experiments as shown in the inset to Fig. 11b.

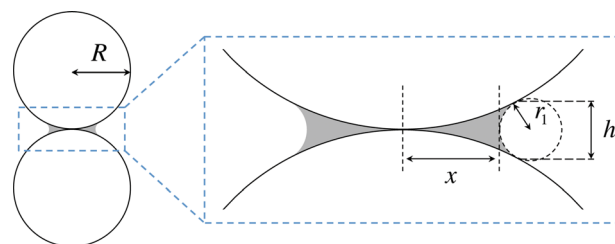


Fig. 13 Cross section schematic of a concave meniscus-shaped capillary bridge keeping two equally sized particles in contact. Meniscus curvature is defined by a circle of radius  $r_1$  and the contact angle is zero.

## 4. Discussion

### 4.1 Percolation, aggregation and arrested coalescence

Our results on the influence of the wetting phase content indicate structural and rheological transitions which are analogous to those observed in wet granular materials at much higher packing fractions.<sup>9,13</sup> Similar changes have also been noted in a very recent work on macroporous ceramics based on capillary suspensions.<sup>88</sup> Here, we consider the nature of these transitions based on the geometric aspects related to the formation of pendular bridges and merging phenomena due to the increase in the wetting fluid volume. The geometry of pendular bridging is depicted in Fig. 13 for spherical particles of equal size (radius  $R$ ) maintained in contact by a fully wetting fluid meniscus (contact angle  $\theta \approx 0$ ) with a circular curvature profile, where  $h$  is the meniscus height,  $x$  is the meniscus radius and  $r_1$  is the meniscus curvature (a zero contact angle implies  $r_1 = x^2/(2(R - x))$  and  $h = \sqrt{3}r_1$ ). Both particle and meniscus volumes can be determined with only two variables ( $R$  and  $h$ ) using the following relations:

$$V_{\text{particle}} = \frac{4}{3}\pi R^3 \quad (4)$$

$$V_{\text{meniscus}} = \pi h^2 \left[ \frac{7h}{12} + \frac{2R}{\sqrt{3}} \right] - \frac{2\pi h^2}{9} \left[ \frac{h^2}{3} + \frac{2hR}{\sqrt{3}} \right]^{1/2} - \frac{\pi h^2}{6} \left( 3R - \frac{h}{2} \right) \quad (5)$$

The size of pendular bridges is primarily controlled by the resulting PEO drop size obtained at the end of the first mixing step. As can be seen in ESI Fig. S9,† our mixing process leads to an average PEO drop diameter of  $\sim 1.2 \mu\text{m}$  prior to the addition of particles. At the lowest PEO concentration probed ( $\varrho \approx 10^{-2}$ ), the quantity of PEO drops is considerably less than that of particles, yet the detection of a yield stress (see Fig. 2b) suggests that a percolated path is already formed. We surmise that such percolated structure does not include all of the particles due to the limited amount of drops needed to form the bridges, where only a fraction of silica particles is connected *via* pendular bridges resulting from the PEO–SP collisions during mixing. In this framework, the initial increase in PEO concentration leads to a greater number of drops, which augments the flow-induced interparticle connectivity while sustaining a nearly constant average meniscus volume. This capillary-driven percolation process continues until all the particles become part of the pendular network, where the increase in network density results in higher strength. This state, referred to as *full pendular bridging*, coincides with the maximum yield stress observed in Fig. 2b. Considering the simplified case of monodisperse particles bridged by equally sized menisci, we can write  $\varrho \approx \phi_{\text{PEO}}/\phi_{\text{SP}} = \bar{z}V_{\text{meniscus}}/(2V_{\text{particle}})$ , where  $\bar{z}$  is the average coordination number, *i.e.* the number of bridging menisci per particle. For percolated networks with a branched structure,  $\bar{z}$  becomes slightly larger than 2 and the latter expression can be approximated by  $\varrho \approx V_{\text{meniscus}}/V_{\text{particle}}$ . Equating the meniscus volume to the average PEO drop volume ( $\bar{V}_{\text{drop}} = 4\pi\bar{R}_{\text{drop}}^3/3$ ) leads to  $\varrho \approx 0.22$ . Although this simple

approach does not consider particles and menisci polydispersities, this  $\varrho$  value is consistent with the results presented in Fig. 2b, where the maximum yield stress is observed for  $\varrho \approx 0.25$ .

At a higher PEO content ( $\varrho > 0.25$ ), the excess of the wetting phase volume contributes to the increase of menisci size and eventually leads to the merging of neighboring menisci. This phenomenon starts locally and induces a transition from the pendular to funicular network morphology, until significant bridge coalescence leads to the formation of compact capillary aggregates as  $\varrho$  increases. Importantly, the surface tension at the PIB–PEO–SP contact line, the Laplace pressure associated with the curvature of the PIB–PEO interface and viscous forces of the PEO bridge all contribute to the dynamic strength of the pendular bridges.<sup>44</sup> Menisci coalescence tends to reduce the contribution of surface tension, especially in the capillary state,<sup>44</sup> while the Laplace pressure contribution remains important. The decrease in yield stress shown in Fig. 2b can thus be attributed to the lowered capillary interactions of the particulate network due to the merging of the binding PEO bridges, similar to wet granular systems.<sup>9,13</sup> In terms of PEO–SP volume ratio, capillary aggregation can start occurring when the meniscus holding two particles in contact becomes large enough so that surrounding particles can join the meniscus periphery (as shown in ESI Fig. S10†). Considering the case of monodisperse particles, the critical meniscus volume  $V_{\text{crit}}$  corresponding to the onset of capillary aggregation can be calculated using eqn (5) for  $r_1 = R$  (see Fig. 13), which results in  $V_{\text{crit}} = \pi(20\sqrt{3} - 9)R^3/6$ . Small compact capillary aggregates composed of six equally sized particles and one meniscus of volume  $V_{\text{crit}}$  can thus be formed when  $\varrho = \sum V_{\text{crit}}/(6V_{\text{particle}})$ , which gives  $\varrho \approx 0.53$  (see dashed line in Fig. 2b). This  $\varrho$  value agrees well with the formation of compact capillary aggregates observed experimentally and with the decrease in yield stress evidenced in Fig. 2b, although the effects of particles and menisci polydispersities are not included in this calculation.

The percolated structures observed in the capillary regime ( $\varrho \geq 0.5$ ) appear to result from two flow-induced processes: the formation of compact capillary aggregates (*primary aggregation*), followed by their percolation (*secondary aggregation*). The latter process involves partial merging of the capillary aggregates, where their raspberry-like drop shape is sustained due to the incomplete coalescence at their interface. Moreover, a more advanced (although still incomplete) merging of the primary aggregates is found when  $\varrho$  increases (compare Fig. 2h–k vs. i–l). Such morphological features are typical of the arrested coalescence phenomena observed for solid-like drops due to the competition between capillary suction and internal drop elasticity.<sup>89,90</sup> This physical phenomenon is particularly consistent in our case, given the high volume fraction of silica particles in the PEO–SP aggregated phase,  $\phi_i$ , which is defined as:

$$\phi_i = \frac{\phi_{\text{SP}}}{\phi_{\text{PEO}} + \phi_{\text{SP}}} = \frac{1}{1 + \varrho} \quad (6)$$

The binary PEO–SP system is found to develop solid-like properties (yield stress and a low-frequency plateau) for particle loadings exceeding 0.40, where  $G_p' \sim \phi_{\text{SP}}^\alpha$  with  $\alpha > 1$  (not shown). This suggests that for  $\phi_i \geq 0.40$  (*i.e.*  $\varrho \leq 1.5$ ), a yield stress is

developed within the drop, and thus the aggregates are expected to predominantly behave like an elastic paste. Accordingly, the low frequency plateau modulus within the aggregates is expected to follow  $G'_p \sim \phi_i^\alpha$ , and thus  $G'_p \sim (1 + \varrho)^{-\alpha}$  using eqn (6). As a result, the increase in  $\varrho$  leads to a lowering of the capillary aggregates elasticity, and thus favors their coalescence, but still leads to an arrested state as long as the elastic energy is high enough to balance the interfacial energy.<sup>89</sup>

#### 4.2 Power-law scalings: effect of interparticular pendular bonding

We now turn to the significant impact of pendular bridging on the elastic modulus plateau and yield stress over the wide range of particle concentrations investigated. The dependence of  $G'_p$  and  $\sigma_y$  on the particle volume fraction  $\phi_{SP}$  for the PIB-SP binary system ( $\varrho = 0$ ) and the PIB-PEO-SP ternary system at full pendular bridging ( $\varrho = 0.16$ ) is presented in Fig. 14. Power-law scalings are found for both the systems above critical values of  $\phi_{SP}$ :

$$G'_p \sim (\phi_{SP})^m \quad (7)$$

$$\sigma_y \sim (\phi_{SP})^v \quad (8)$$

Such laws are ubiquitous in gel-like complex fluid systems.<sup>72</sup> In our case, these solid-like properties appear around  $\phi_{SP} = 0.25$  in the absence of PEO (which may be regarded as a PIB-SP suspension-to-paste transition, *i.e.* the suspension becomes

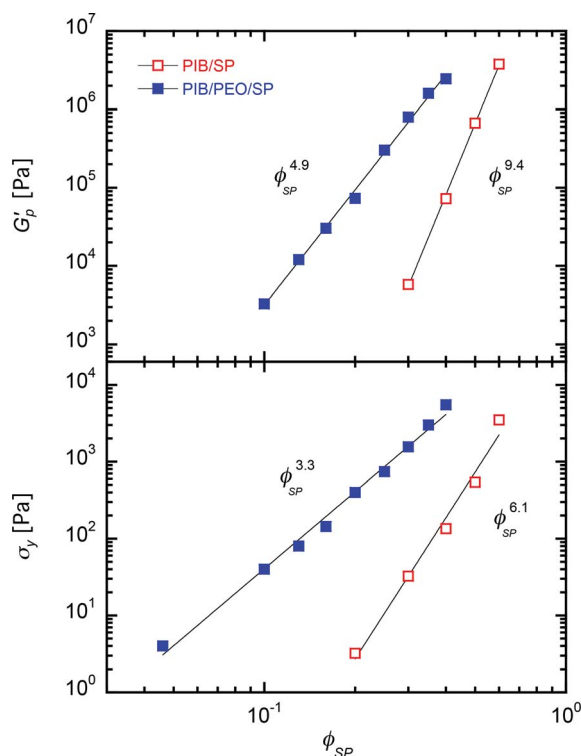


Fig. 14 Scaling laws of  $G'_p$  and  $\sigma_y$  for binary ( $\varrho = 0$ , red open squares) and ternary systems ( $\varrho = 0.16$ , blue filled squares).

solid-like at rest due to increased particle interactions when the particle volume fraction gets closer to the concentrated regime, but can behave like a liquid under deformation<sup>37</sup>), and around  $\phi_{SP} = 0.04$  in the case of the ternary system (corresponding to the pendular percolation threshold). The scaling exponents found for the pendular gels ( $m = 4.9$  and  $v = 3.3$ ) are close to those found for colloidal silica gels,<sup>91–95</sup> and strongly differ from the values obtained for the PIB-SP pastes ( $m = 9.4$  and  $v = 6.1$ ). For both systems, the values of  $G'_p$  (as well as those of  $\sigma_y$ ) approach each other at very high  $\phi_{SP}$ , although a significant gap is observed at fixed  $\phi_{SP}$  values over the investigated range ( $G'_p$  and  $\sigma_y$  are typically ten- to twenty-fold higher for pendular gels compared to PIB-SP pastes at the same  $\phi_{SP}$ ). This great increase in elasticity and yield stress denotes an increase in interparticle attractive energy<sup>2</sup> due to the pendular bonds. We also note that the transition from an open branched gel morphology to a macroporous structure (Fig. 6) observed for the ternary system for  $\phi_{SP} \geq 0.35$  does not affect the scaling of  $G'_p$  and  $\sigma_y$ .

Other parameters, like the contact angle  $\theta$ , the interfacial tension between the two immiscible liquids  $\Gamma$ , the particle radius  $R$  and the viscosity of the binding liquid  $\eta_b$ , should also have a significant influence on the yield stress of pendular systems. Indeed, the particle size is already known to have a great effect on the strength of wet granular materials, where the yield stress increases when the particle size decreases or when the polydispersity of particle increases.<sup>44</sup> For oil/water/glass particle pendular systems, Koos *et al.*<sup>7</sup> have shown that  $\sigma_y \sim R^{-1}$ .

#### 4.3 Analogy of pendular networks to attractive colloidal gels

The robust gel-like dynamics and yielding behavior found for our pendular gels result from the flow-induced network structure based on adhesive capillary interactions. However, very similar properties have been widely reported for attractive colloidal gels, where self-assembly of the colloidal phase occurs when the attractive energy exceeds the thermal energy.

Fractal scaling theories<sup>73,95</sup> have been introduced to link the solid-like rheology of attractive colloidal gels to their network geometry. Piau *et al.*<sup>95</sup> proposed a scaling approach that proved successful for colloidal silica gels<sup>95</sup> and colloidal disk gels.<sup>96</sup> Their concept for the network elasticity relies on the free-energy associated with the fractal domains of size  $\xi$ . Using de Gennes' scaling concept for polymer gels, the average floc size is related to the particle volume fraction  $\phi$  by  $\xi \sim \phi^{1/(d_f-3)}$ , which leads to the following scaling laws:

$$G'_p \sim \phi^{5/(3-d_f)} \quad (9)$$

$$\sigma_y \sim \phi^{4/(3-d_f)} \quad (10)$$

In this framework, the measured exponents  $m$  and  $v$  (from eqn (7) and (8)) are expected to satisfy  $m/v = 5/4$ . The actual ratio found in our case is 1.48, which is somewhat higher than expected. Nevertheless, applying this scaling theory to our pendular gels, we find  $d_f \approx 1.98$  (from eqn (9)) and  $d_f \approx 1.79$  (from eqn (10)). These values lie between those associated with the cluster-cluster aggregation model and the reaction-limited aggregation model.<sup>73</sup> This fractal dimension is also close to that

found for wet granular gases<sup>45</sup> ( $d_f \approx 2.0$ ). Although the fractal nature of pendular gels is peripheral to our study, it should certainly be considered in greater details for future investigations using complementary approaches.

#### 4.4 Compositional state diagram

A schematic diagram representing the main structures associated with the changes in the two composition parameters, *i.e.* the volume fractions of silica particles and PEO, is shown in Fig. 15a. In the case of PIB-SP binary systems (bottom row in Fig. 15a), particles start to interact when  $\phi_{SP}$  is high enough to significantly reduce interparticle separation. At low  $\varrho$  (middle row in Fig. 15a), the PEO menisci behave like gelators by bridging the particles through strong capillary attractions. The ternary structures start as isolated particle flocs for low  $\phi_{SP}$ ,

which can grow into sample-spanning structures as  $\phi_{SP}$  increases, eventually leading to the formation of heterogeneous macroporous pendular structures. At higher  $\varrho$  (top row in Fig. 15a), the menisci coalesce and compact capillary aggregates are formed. Hierarchical clustering is then observed due to partial coalescence of the capillary aggregates, which can form a percolated path throughout the sample.

We aim to delineate how these structural changes result in a transition from a fluid-like flow behavior to the solid-like state by plotting a compositional state diagram ( $\varrho$  vs.  $\phi_{SP}$ ) in Fig. 15b. Note that the limiting case of random close packing for monodisperse spheres is employed ( $\phi_{RCP} \approx 0.639$ ), although a higher value should be expected due to the particle polydispersity. The fluid-gel frontier in Fig. 15b represents the rheological percolation threshold for a fixed  $\varrho$  value. For  $\varrho = 0$ , a suspension-to-paste transition occurs around  $\phi_{SP} = 0.25$ . As  $\varrho$  starts to increase, a very sharp decrease in the percolation threshold is found (down to  $\phi_{SP} = 0.04$  for  $\varrho = 0.16$ ), corresponding to the formation of a pendular network. Further increase of  $\varrho$  successively leads to funicular and capillary aggregate morphologies (these transitions are indicated at fixed  $\varrho$  values regardless of  $\phi_{SP}$  in Fig. 15b, based on experimental observations at  $\phi_{SP} = 0.1$ , which is a conjectural assumption). Given that the network is formed by compact capillary aggregates rather than particles themselves when  $\varrho \geq 0.4$ , we speculate that the percolation threshold tends to increase with  $\varrho$  in this region of the diagram. It should also be noted that our study is restrained to  $0 \leq \varrho \leq 1$ , although the ternary system might return to a fluid-like behavior for  $\varrho > 1$ , especially after phase inversion occurs.

## 5. Conclusions and outlook

We have reported on the flow-induced assembly phenomena in ternary blends composed of two immiscible polymers and silica particles over a wide region of the compositional space, where the particles are almost completely wetted by one of the polymer phases. Even at volume fractions as low as 0.002, the wetting polymer phase enables the formation of a percolated path *via* the capillary bridging of particles, giving way to the solid-like behavior of the ternary blends. Further increase of the wetting phase content extends the connectivity of the pendular network until the particle-bridging menisci start to coalesce, eventually resulting in the formation of compact capillary aggregates. Merging of the menisci primarily depends on the mixing flow conditions and geometrical aspects, and is triggered above a critical value of the wetting phase to the particle volume ratio  $\varrho$ . Interestingly, our results reveal that two types of percolation are distinguishable depending on  $\varrho$ : silica particles are bridged through pendular percolation for low  $\varrho$  values, whereas compact capillary aggregates serve as building blocks for the formation of a sample-spanning network through their arrested coalescence in the higher  $\varrho$  regime. These morphological transitions are accompanied by a rise and fall of the yield stress, analogous to wet granular media, due to the decreased capillary interactions and change in percolating structure. The yield stress reaches the maximum at full pendular bridging for  $\varrho$  close to 0.25.

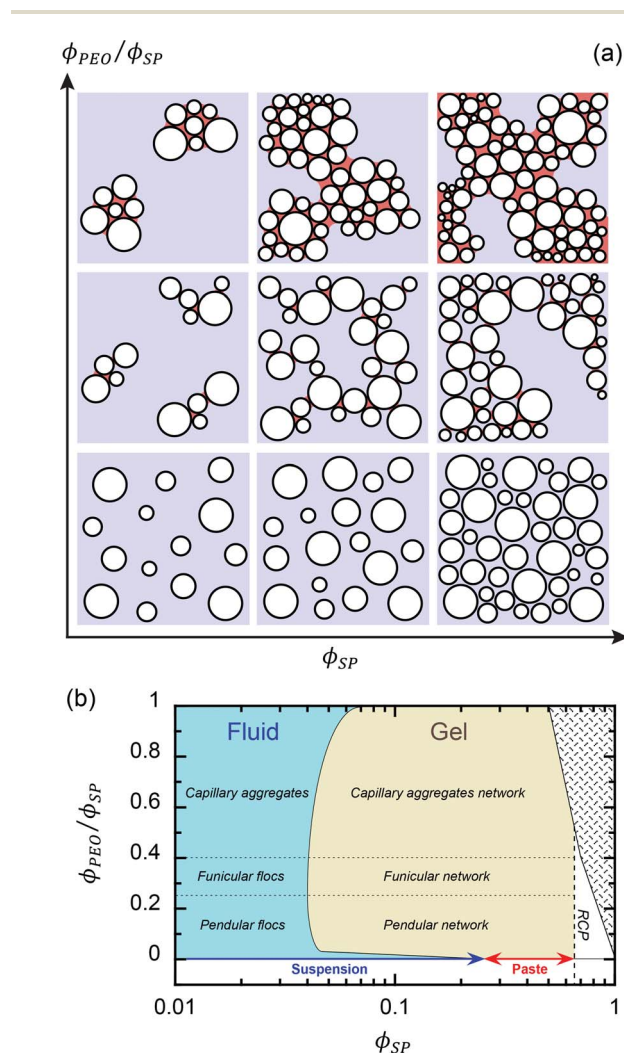


**Fig. 15** (a) Schematic overview of the structural transitions resulting from variations in the particle volume fraction  $\phi_{SP}$  and wetting phase-particle volume ratio  $\varrho = \phi_{PEO}/\phi_{SP}$ . (b) Compositional state diagram. The textured area in the upper-right corner of (b) represents an unphysical composition region of the ternary system (the sum of the three volume fractions cannot exceed 1), while the vertical dashed line marks the random close packing fraction for monodisperse spheres ( $\phi_{RCP} \approx 0.639$ ).

This value should arguably depend on the relative meniscus/particle size and particle size distribution. Our study also includes the first detailed investigation on the linear/nonlinear viscoelasticity and yielding of pendular gels. Such systems exhibit a significant increase in elasticity and yield stress, as well as a shortening of the linear viscoelastic domain and a lower percolation threshold compared to the non-bridged particle suspensions and pastes. All of these effects result from an increase in attractive interactions between the particles, where the dispersed drops of the wetting phase act as gelators *via* the meniscus bridging of the particles during mixing.

Finally, we summarize some open questions concerning this class of soft materials. Our investigations on nonlinear viscoelasticity require more detailed studies on strain thinning and yielding dynamics of pendular systems. In particular, the questions of flow-induced restructuration and heterogeneous flow during strain-induced and stress-induced transients remain crucial. In terms of capillary attractions, how does the fluid–solid transition change with the contact angle, and can it be unified on a jamming phase diagram? In addition, the apparent similarities of these ternary systems with wet granular materials raises the possibility of a theoretical framework that could unify the flow behavior of fluid–fluid–solid particle ternary systems and wet granular media. Further exploration of the ternary composition diagram promises new progress on flow-induced ternary structures, such as the formation of bicontinuous networks and phase inversion phenomena, and warrants future studies beyond the scope of the present work.

## Acknowledgements

Financial support for this research was provided by the National Science Foundation (NSF-CBET grant no. 0932901 and 1336311). We thank Craig Maloney, Carnegie Mellon University, for insightful discussions. We also thank Yungchieh Lai and Götz Vesper for their kind help with HR-TEM observations, along with Jason Devlin, Morgan Jessup, and Mark Ross, Center for Biological Imaging at the University of Pittsburgh, for assistance with confocal imaging.

## References

- 1 E. Zaccarelli, *J. Phys.: Condens. Matter*, 2007, **19**, 323101.
- 2 V. Prasad, V. Trappe, A. D. Dinsmore, P. N. Segre, L. Cipelletti and D. A. Weitz, *Faraday Discuss.*, 2003, **123**, 1–12.
- 3 P. C. F. Møller, J. Mewis and D. Bonn, *Soft Matter*, 2006, **2**, 274–283.
- 4 E. Koos and N. Willenbacher, *Science*, 2011, **331**, 897–900.
- 5 T. Domenech and S. Velankar, *Rheol. Acta*, 2014, **53**, 593–605.
- 6 S. Van Kao, L. E. Nielsen and C. T. Hill, *J. Colloid Interface Sci.*, 1975, **53**, 367–373.
- 7 E. Koos, J. Johannsmeier, L. Schwebler and N. Willenbacher, *Soft Matter*, 2012, **8**, 6620–6628.
- 8 S. J. Heidlebaugh, T. Domenech, S. V. Iasella and S. S. Velankar, *Langmuir*, 2014, **30**, 63–74.
- 9 M. Scheel, R. Seemann, M. Brinkmann, M. Di Michiel, A. Sheppard, B. Breidenbach and S. Herminghaus, *Nat. Mater.*, 2008, **7**, 189–193.
- 10 S. Strauch and S. Herminghaus, *Soft Matter*, 2012, **8**, 8271–8280.
- 11 D. J. Hornbaker, R. Albert, I. Albert, A. L. Barabasi and P. Schiffer, *Nature*, 1997, **387**, 765.
- 12 N. Mitarai and F. Nori, *Adv. Phys.*, 2006, **55**, 1–45.
- 13 P. C. F. Møller and D. Bonn, *Europhys. Lett.*, 2007, **80**, 38002.
- 14 W. Pietsch, *Agglomeration Processes: Phenomena, Technologies, Equipment*, Wiley, Weinheim, 2008.
- 15 S. M. Iveson, J. D. Litster, K. Hapgood and B. J. Ennis, *Powder Technol.*, 2001, **117**, 3–39.
- 16 C. Py, P. Reverdy, L. Doppler, J. Bico, B. Roman and C. N. Baroud, *Phys. Rev. Lett.*, 2007, **98**, 156103.
- 17 F. Li and A. Stein, *J. Am. Chem. Soc.*, 2009, **131**, 9920–9921.
- 18 E. Duguet, A. Desert, A. Perro and S. Ravaine, *Chem. Soc. Rev.*, 2011, **40**, 941–960.
- 19 T. Brunschweiler, G. Schlottig, S. Ni, Y. Liu, J. V. Goicochea, J. Zurcher and H. Wolf, *Proceedings of the 45th International Symposium on Microelectronics*, San Diego, California USA, 2012.
- 20 D. J. Eichelsdoerfer, K. A. Brown and C. A. Mirkin, *Soft Matter*, 2014, **10**, 5603–5608.
- 21 H.-J. Butt, *Science*, 2011, **331**, 868–869.
- 22 W. Ramsden, *Proc. R. Soc. London*, 1903, **72**, 156–164.
- 23 S. U. Pickering, *J. Chem. Soc.*, 1907, **91**(92), 2001–2021.
- 24 J. Vermant, G. Cioccolo, K. Golapan Nair and P. Moldenaers, *Rheol. Acta*, 2004, **43**, 529–538.
- 25 P. Thareja and S. Velankar, *Rheol. Acta*, 2007, **46**, 405–412.
- 26 L. Elias, F. Fenouillot, J. C. Majesté, P. Alcouffe and P. Cassagnau, *Polymer*, 2008, **49**, 4378–4385.
- 27 F. Fenouillot, P. Cassagnau and J. C. Majesté, *Polymer*, 2009, **50**, 1333–1350.
- 28 P. Thareja, K. Moritz and S. Velankar, *Rheol. Acta*, 2010, **49**, 285–298.
- 29 S. P. Nagarkar and S. S. Velankar, *Soft Matter*, 2012, **8**, 8464–8477.
- 30 M. N. Lee, H. K. Chan and A. Mohraz, *Langmuir*, 2011, **28**, 3085–3091.
- 31 K. Stratford, R. Adhikari, I. Pagonabarraga, J.-C. Desplat and M. E. Cates, *Science*, 2005, **309**, 2198–2201.
- 32 E. M. Herzig, K. A. White, A. B. Schofield, W. C. K. Poon and P. S. Clegg, *Nat. Mater.*, 2007, **6**, 966–971.
- 33 M. E. Cates and P. S. Clegg, *Soft Matter*, 2008, **4**, 2132–2138.
- 34 J. A. Witt, D. R. Mumm and A. Mohraz, *Soft Matter*, 2013, **9**, 6773–6780.
- 35 P. Coussot, *Rheometry of Pastes, Suspensions, and Granular Materials: Applications in Industry and Environment*, Wiley, 2005.
- 36 S. P. Meeker, R. T. Bonnecaze and M. Cloitre, *Phys. Rev. Lett.*, 2004, **92**, 198302.
- 37 P. Coussot, *Soft Matter*, 2007, **3**, 528–540.
- 38 V. Trappe and D. A. Weitz, *Phys. Rev. Lett.*, 2000, **85**, 449–452.
- 39 P. Coussot, *Phys. Rev. Lett.*, 1995, **74**, 3971–3974.
- 40 C. R. Lin and W. J. Chen, *Colloid Polym. Sci.*, 1999, **277**, 1019–1025.

- 41 J. R. Seth, L. Mohan, C. Locatelli-Champagne, M. Cloitre and R. T. Bonnecaze, *Nat. Mater.*, 2011, **10**, 838–843.
- 42 L. Mohan, C. Pellet, M. Cloitre and R. Bonnecaze, *J. Rheol.*, 2013, **57**, 1023–1046.
- 43 M. Marić and C. W. Macosko, *Polym. Eng. Sci.*, 2001, **41**, 118–130.
- 44 S. M. Iveson, J. A. Beathe and N. W. Page, *Powder Technol.*, 2002, **127**, 149–161.
- 45 S. Ulrich, T. Aspelmeier, A. Zippelius, K. Roeller, A. Fingerle and S. Herminghaus, *Phys. Rev. E: Stat., Nonlinear, Soft Matter Phys.*, 2009, **80**, 031306.
- 46 H. H. Winter and F. Chambon, *J. Rheol.*, 1986, **30**, 367–382.
- 47 M. Laurati, G. Petekidis, N. Koumakis, F. Cardinaux, A. B. Schofield, J. M. Brader, M. Fuchs and S. U. Egelhaaf, *J. Chem. Phys.*, 2009, **130**, 134907.
- 48 A. P. R. Eberle, R. Castañeda-Priego, J. M. Kim and N. J. Wagner, *Langmuir*, 2012, **28**, 1866–1878.
- 49 M. Laurati, S. U. Egelhaaf and G. Petekidis, *J. Rheol.*, 2011, **55**, 673–706.
- 50 T. G. Mason and D. A. Weitz, *Phys. Rev. Lett.*, 1995, **75**, 2770–2773.
- 51 N. Koumakis and G. Petekidis, *Soft Matter*, 2011, **7**, 2456–2470.
- 52 B. M. Erwin, M. Cloitre, M. Gauthier and D. Vlassopoulos, *Soft Matter*, 2010, **6**, 2825–2833.
- 53 S. Z. Ren and C. M. Sorensen, *Phys. Rev. Lett.*, 1993, **70**, 1727–1730.
- 54 L. Berthier and G. Biroli, *Rev. Mod. Phys.*, 2011, **83**, 587–645.
- 55 K. A. Dawson, *Curr. Opin. Colloid Interface Sci.*, 2002, **7**, 218–227.
- 56 K. Hyun, M. Wilhelm, C. O. Klein, K. S. Cho, J. G. Nam, K. H. Ahn, S. J. Lee, R. H. Ewoldt and G. H. McKinley, *Prog. Polym. Sci.*, 2011, **36**, 1697–1753.
- 57 C. Derec, G. Ducouret, A. Ajdari and F. Lequeux, *Phys. Rev. E: Stat., Nonlinear, Soft Matter Phys.*, 2003, **67**, 061403.
- 58 V. Carrier and G. Petekidis, *J. Rheol.*, 2009, **53**, 245–273.
- 59 F. Renou, J. Stellbrink and G. Petekidis, *J. Rheol.*, 2010, **54**, 1219–1242.
- 60 J.-C. Majesté, C. Carrot, B. Olalla and R. Fulchiron, *Macromol. Theory Simul.*, 2012, **21**, 113–119.
- 61 K. Miyazaki, H. M. Wyss, D. A. Weitz and D. R. Reichman, *Europhys. Lett.*, 2006, **75**, 915–921.
- 62 R. Ewoldt, P. Winter, J. Maxey and G. McKinley, *Rheol. Acta*, 2010, **49**, 191–212.
- 63 N. Koumakis, A. Pamvouxoglou, A. S. Poulos and G. Petekidis, *Soft Matter*, 2012, **8**, 4271–4284.
- 64 A. Poulos, J. Stellbrink and G. Petekidis, *Rheol. Acta*, 2013, **52**, 785–800.
- 65 H. K. Chan and A. Mohraz, *Phys. Rev. E: Stat., Nonlinear, Soft Matter Phys.*, 2012, **85**, 041403.
- 66 Z. Shao, A. S. Negi and C. O. Osuji, *Soft Matter*, 2013, **9**, 5492–5500.
- 67 M. Laurati, S. U. Egelhaaf and G. Petekidis, *J. Rheol.*, 2014, **58**, 1395–1417.
- 68 W. Herschel and R. Bulkley, *Am. Soc. Test. Mater., Proc.*, 1926, **26**, 621–633.
- 69 D. Quemada, *Rheol. Acta*, 1977, **16**, 82–94.
- 70 R. S. Farr and R. D. Groot, *J. Chem. Phys.*, 2009, **131**, 244104.
- 71 E. Santiso and E. A. Müller, *Mol. Phys.*, 2002, **100**, 2461–2469.
- 72 P. Cassagnau, *Polymer*, 2008, **49**, 2183–2196.
- 73 W.-H. Shih, W. Y. Shih, S.-I. Kim, J. Liu and I. A. Aksay, *Phys. Rev. A*, 1990, **42**, 4772–4779.
- 74 C. D. Willett, M. J. Adams, S. A. Johnson and J. P. K. Seville, *Langmuir*, 2000, **16**, 9396–9405.
- 75 S. Cai and B. Bhushan, *Philos. Trans. R. Soc., A*, 2008, **366**, 1627–1647.
- 76 P. Coussot, Q. D. Nguyen, H. T. Huynh and D. Bonn, *J. Rheol.*, 2002, **46**, 573–589.
- 77 F. Da Cruz, F. Chevoir, D. Bonn and P. Coussot, *Phys. Rev. E: Stat., Nonlinear, Soft Matter Phys.*, 2002, **66**, 051305.
- 78 J. Sprakel, S. B. Lindström, T. E. Kodger and D. A. Weitz, *Phys. Rev. Lett.*, 2011, **106**, 248303.
- 79 S. B. Lindstrom, T. E. Kodger, J. Sprakel and D. A. Weitz, *Soft Matter*, 2012, **8**, 3657–3664.
- 80 P. Coussot, H. Tabuteau, X. Chateau, L. Tocquer and G. Ovarlez, *J. Rheol.*, 2006, **50**, 975–994.
- 81 F. Caton and C. Baravian, *Rheol. Acta*, 2008, **47**, 601–607.
- 82 P. H. T. Uhlherr, J. Guo, C. Tiu, X. M. Zhang, J. Z. Q. Zhou and T. N. Fang, *J. Non-Newtonian Fluid Mech.*, 2005, **125**, 101–119.
- 83 T. Gibaud, D. Frelat and S. Manneville, *Soft Matter*, 2010, **6**, 3482–3488.
- 84 T. Divoux, C. Barentin and S. Manneville, *Soft Matter*, 2011, **7**, 8409–8418.
- 85 V. Grenard, T. Divoux, N. Taberlet and S. Manneville, *Soft Matter*, 2014, **10**, 1555–1571.
- 86 M. Siebenbürger, M. Ballauff and T. Voigtmann, *Phys. Rev. Lett.*, 2012, **108**, 255701.
- 87 E. A. Jagla, *Phys. Rev. E: Stat., Nonlinear, Soft Matter Phys.*, 2011, **83**, 046119.
- 88 J. Dittmann and N. Willenbacher, *J. Am. Ceram. Soc.*, 2014, 3787–3792.
- 89 A. B. Pawar, M. Caggioni, R. W. Hartel and P. T. Spicer, *Faraday Discuss.*, 2012, **158**, 341–350.
- 90 K. Boode and P. Walstra, *Colloids Surf., A*, 1993, **81**, 121–137.
- 91 R. S. Chahal and L. E. St Pierre, *Macromolecules*, 1969, **2**, 193–197.
- 92 M. Kolb, *Phys. Rev. Lett.*, 1984, **53**, 1653–1656.
- 93 M. I. Aranguren, E. Mora, J. V. DeGroot and C. W. Macosko, *J. Rheol.*, 1992, **36**, 1165–1182.
- 94 S. A. Khan and N. J. Zoeller, *J. Rheol.*, 1993, **37**, 1225–1235.
- 95 J.-M. Piau, M. Dorget, J.-F. Paliarne and A. Pouchelon, *J. Rheol.*, 1999, **43**, 305–314.
- 96 A. Loiseau and J.-F. Tassin, *Macromolecules*, 2006, **39**, 9185–9191.